Nanoscale

PAPER

View Article Online
View Journal | View Issue

Cite this: *Nanoscale*, 2019, **11**, 21227

Multifunctional temozolomide-loaded lipid superparamagnetic nanovectors: dual targeting and disintegration of glioblastoma spheroids by synergic chemotherapy and hyperthermia treatment†

Attilio Marino,*‡[a] Alice Camponovo,‡[b] Andrea Degl'Innocenti,[a] Martina Bartolucci,[c] Christos Tapeinos,[a] Chiara Martinelli,[a] Daniele De Pasquale,[a,d] Francesca Santoro,[e] Valentina Mollo,[e] Satoshi Arai,[f,g] Madoka Suzuki,[h,i] Yoshie Harada,[h] Andrea Petretto[c] and Gianni Ciofani *[a,b]

Aiming at finding new solutions for fighting glioblastoma multiforme, one of the most aggressive and lethal human cancer, here an *in vitro* validation of multifunctional nanovectors for drug delivery and hyperthermia therapy is proposed. Hybrid magnetic lipid nanoparticles have been fully characterized and tested on a multi-cellular complex model resembling the tumor microenvironment. Investigations of cancer therapy based on a physical approach (namely hyperthermia) and on a pharmaceutical approach (by exploiting the chemotherapeutic drug temozolomide) have been extensively carried out, by evaluating its antiproliferative and pro-apoptotic effects on 3D models of glioblastoma multiforme. A systematic study of transcytosis and endocytosis mechanisms has been moreover performed with multiple complimentary investigations, besides a detailed description of local temperature increments following hyperthermia application. Finally, an in-depth proteomic analysis corroborated the obtained findings, which can be summarized in the preparation of a versatile, multifunctional, and effective nanoplatform able to overcome the blood–brain barrier and to induce powerful anti-cancer effects on *in vitro* complex models.

Received 16th September 2019,
Accepted 19th October 2019

DOI: 10.1039/c9nr07976a

rsc.li/nanoscale

Introduction

In the current clinical practice, the golden standard therapy against glioblastoma multiforme (GBM) relies on surgical resection followed by the combination of radiotherapy and chemotherapy, usually performed with temozolomide (TMZ).[1] The poor prognosis of this pathology (12–15 months) is mainly associated with the usual recurrence of GBM after these treatments. Moreover, the low efficacy of the approach is related to the impossibility of completely removing GBM cells by surgery, the inability to deliver an effective dose of TMZ to the cancer mass, and the elevated aggressiveness of the GBM cells.[2] Furthermore, GBM is the most angiogenic brain tumor,[3] and cannot be completely resected due to its indistinct margins.[4] Groups of cells that are removed by surgery develop the so-called microscopic foci; these cell populations are extremely difficult to be detected, resist the current chemotherapy/radiotherapy approaches, and regenerate the tumor mass in a few months.[5] In this context, the current strategies dedicated to prevent the GBM recurrence require precise targeting, at both

[a]*Istituto Italiano di Tecnologia, Smart Bio-Interfaces, Viale Rinaldo Piaggio 34, 56025 Pontedera, Italy. E-mail: attilio.marino@iit.it, gianni.ciofani@iit.it*
[b]*Politecnico di Torino, Department of Mechanical and Aerospace Engineering, Corso Duca degli Abruzzi 24, 10129 Torino, Italy*
[c]*IRCCS Istituto Giannina Gaslini, Via Gerolamo Gaslini 5, 16147 Genova, Italy*
[d]*Scuola Superiore Sant'Anna, The Biorobotics Institute, Viale Rinaldo Piaggio 34, 56025 Pontedera, Italy*
[e]*Istituto Italiano di Tecnologia, Center for Advanced Biomaterials for Health Care, Largo Barsanti e Matteucci 53, 80125 Naples, Italy*
[f]*Kanazawa University, Nano Life Science Institute (WPI-NanoLSI), Kakuma-Machi, 920-1192 Kanazawa, Japan*
[g]*Waseda University, Research Institute for Science and Engineering, 3-4-1 Ohkubo, Shinjuku-ku, 169-8555 Tokyo, Japan*
[h]*Osaka University, Institute for Protein Research, 3-2 Yamadaoka, Suita-Shi, 565-0871 Osaka, Japan*
[i]*PRESTO, Japan Science and Technology Agency (JST), 4-1-8 Honcho, Kawaguchi, 332-0012 Saitama, Japan*

†Electronic supplementary information (ESI) available. See DOI: 10.1039/c9nr07976a

‡These authors equally contributed to this work.

the anatomical and cellular levels, of therapeutic/theranostic agents against the microscopic foci.

The recent development of nanotechnology promises to revolutionize the delivery of chemotherapeutic agents and of other pharmacologically/biologically active compounds across the blood–brain barrier (BBB) and towards cancer cells.[6,7] Beside the passive phenomenon of nanomaterial accumulation in the tumor sites due to its highly fenestrated microcapillaries, other active mechanisms for the systemic delivery of theranostic nanomaterials to brain cancer cells have been recently developed and validated.[8] Promising approaches include the exploitation of magnetically responsive nanovectors for anatomical targeting through an external magnetic guidance,[9] permeability enhancers for the transient opening of the BBB in specific brain areas,[10] and molecular "Trojan horses" for the dual targeting of BBB and GBM cells.[11] In this regard, magnetically responsive nanocarriers represent a multifunctional platform with targeting and diagnostic capabilities, adopted for the remote delivery of drugs and of magnetothermal stimuli to cancer cells.[9]

Superparamagnetic nanoparticles are single-domain magnetic nanostructures characterized by excellent magnetic susceptibility; when exposed to alternating magnetic fields (AMF), they efficiently generate heat through Nèel's and Brown's relaxation phenomena. Single-domain magnetic nanoparticles do not show remanence and coercivity, thus preventing their aggregation and ensuring the maintenance of their superparamagnetic behaviour.[12,13] Superparamagnetic iron oxide nanoparticles (SPIONs) are magnetic nanostructures with excellent biocompatibility, and they have been approved by the Food and Drug Administration (FDA) for the clinical treatment of anemia associated with chronic kidney disease.[14] Moreover, SPIONs have been successfully exploited in many different clinical trials for the remote hyperthermal treatment of cancer cells in response to alternating magnetic fields (AMF) and as contrast agents for magnetic resonance imaging (MRI).[15] As a supplementary function, SPIONs can be incorporated into thermosensitive nanovectors for the controlled release of specific anticancer drugs/molecules.[16]

In this work, the functionalization of SPION- and TMZ-loaded lipid magnetic nanovectors (LMNVs) with an antibody against the transferrin receptor (TfR) for the dual targeting of the endothelial cells of the BBB and of GBM cells is reported. The targeting efficiency of the functionalized nanovectors (AbLMNVs) has been demonstrated on a multicellular organoid system in the presence of an *in vitro* BBB model. Transcytosis of functionalized nanovectors through endothelial cells and their penetration into GBM spheroids have been verified and quantified through flow cytometry analysis and several imaging techniques. Moreover, the lipid component of the functionalized nanovectors has been modified with a lipophilic temperature-sensitive fluorescent dye to monitor the intraparticle temperature in response to the AMF exposure. Chronic AMF treatments of GBM spheroids targeted with the functionalized nanovectors, either plain or loaded with TMZ, were carried out and their elevated potential to induce spheroid disintegration, cell necrosis and apoptosis was revealed. Finally, the magnetothermal ability of nanovectors was successfully tested on a *post-mortem* animal brain tissue.

Results

AbLMNV characterization

Lipid magnetic nanovectors (LMNVs) loaded with superparamagnetic iron oxide nanoparticles (SPIONs) were functionalized with an antibody against the transferrin receptor (anti-TfR Ab) in order to achieve a dual targeting of the endothelial cells of the BBB and of the GBM cells, as both these types of cells highly express the TfR.[17,18] The scheme of the nanovector functionalization, TEM imaging, and analysis of the Ab functionalization efficiency are shown in Fig. 1. Fig. 1a depicts the surface modification, which was achieved by exploiting a biotin–streptavidin interaction between biotin-functionalized 1,2-distearoyl-*sn-glycero*-3-phosphoethanolamine (DSPE)-conjugated poly(ethylene glycol) (biotin-PEG-DSPE) and streptavidin-conjugated Ab. TEM imaging of the Ab-functionalized nanovectors (AbLMNVs) is reported in Fig. 1b and c. AbLMNVs are characterized by a spheroidal morphology and a diameter of 36 ± 25 nm; the presence of the SPIONs can be appreciated owing to their higher electron-density with respect to the lipid matrix where they are embedded. The average hydrodynamic diameter (D) and the polydispersity index (PDI) of the AbLMNVs were, respectively, D = 101.3 ± 1.1 nm and PDI = 0.19 ± 0.01 in water, and D = 94.7 ± 1.0 nm and PDI = 0.48 ± 0.01 in complete medium. Further details concerning the physicochemical and magnetic characterization of the nanovectors can be found in a previous study by our group.[16]

The nanovector functionalization was confirmed by SDS-PAGE (Fig. 1d). After the molecular weight indicator, the first three lanes represent the bands of the free Ab (5, 1 and 0 μg of the Ab are loaded from left to right, respectively); the fourth lane is instead loaded with AbLMNV (30 μl of a 5 mg ml^{-1} dispersion). The characteristic bands of the anti-TfR Ab can be found in the AbLMNV sample, therefore confirming the successful functionalization of the particles. The last two lanes consist of two negative controls (biotin-LMNVs and LMNVs, respectively, from left to right), which do not present any band, as expected. The correlation between the intensity of the band attributed to the Ab light chain (MW ~ 25 kDa) and the amount of the free Ab loaded in the gel is shown in the ESI (Fig. S1†); owing to this calibration curve, an amount of 1.9 μg of the Ab was estimated in 30 μl of a 5 mg ml^{-1} AbLMNV dispersion. This result indicated that 42% of the Ab used in the functionalization reaction successfully associated with the nanovectors.

Dual targeting and magnetic guidance of functionalized AbLMNVs

The dual targeting of AbLMNVs was investigated by using a multicellular model of the blood–brain barrier (BBB, with

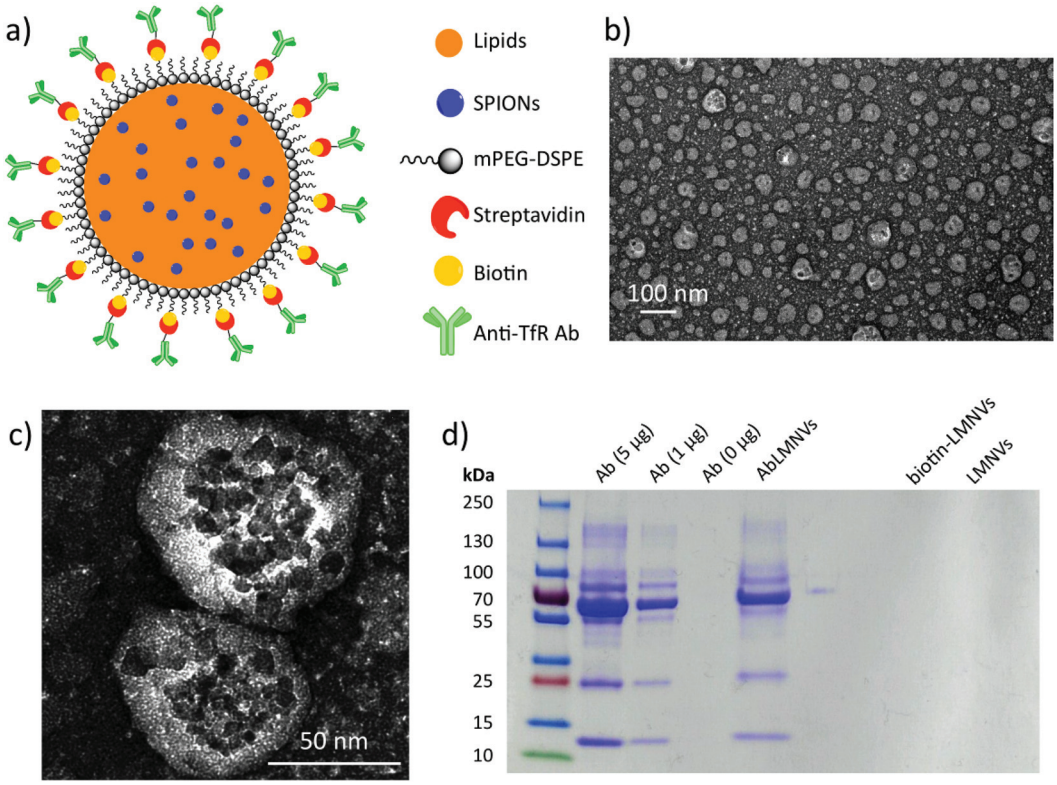

Fig. 1 (a) Scheme showing lipid magnetic nanovectors (LMNVs) loaded with superparamagnetic iron oxide nanoparticles (SPIONs) and functionalized with an anti-transferrin receptor antibody (anti-TfR Ab). (b) Low magnification and (c) high magnification transmission electron microscopy (TEM) images of functionalized nanovectors (AbLMNVs). (d) Identification of the anti-TfR Ab on AbLMNVs: SDS-PAGE stained with Coomassie Brilliant Blue R.

brain endothelial cells and astrocytes) separating a luminal compartment from an abluminal compartment, the latter of which contains cancer spheroids (Fig. 2). The scheme of the multicellular organoid system used for studying the BBB crossing and the following GBM targeting of the nanovectors is shown in Fig. 2a. Astrocytes and endothelial cells of the BBB are respectively seeded on the abluminal and luminal sides of the membrane separating the two compartments. Endothelial cells of the BBB model developed a dense monolayer and highly expressed *zonula occludens-1* (ZO-1), a specific marker of the tight junctions; trans-endothelial electrical resistance (TEER) between luminal and abluminal compartments was 99.0 ± 6.6 Ω cm^2 after 4 days of culture. The complete formation of the endothelial layer on the luminal side of the BBB can be appreciated by the confocal laser scanning microscopy imaging of ZO-1 provided in the ESI (Fig. S2†).

Plain or functionalized nanovectors (LMNVs or AbLMNVs), fluorescently labeled with DiO, were incubated in the luminal compartment and their crossing through the BBB in the abluminal chamber was investigated in the presence or absence of a static magnetic field (SMF), at different time points (24, 48 and 72 h; Fig. 2b). In this study, we observed that the presence of SMF and the functionalization with the anti-TfR Ab were able to independently and synergistically promote the BBB crossing. Regarding the samples non-treated with SMF, the concentration of LMNVs in the abluminal compartments at 48 h (3.0 ± 1.3 μg) and 72 h (7.1 ± 1.3 μg) was significantly lower with respect to that of AbLMNVs measured at 48 h (7.1 ± 0.7 μg; $p < 0.05$) and 72 h (13.3 ± 1.3 μg; $p < 0.05$). No significant differences in BBB crossing were detected for LMNVs and AbLMNVs at 24 h ($p > 0.05$%). The presence of SMF induced a remarkable increase of BBB crossing of both LMNVs (8.4 ± 6.9 μg at 24 h, 22.2 ± 5.9 μg at 48 h, and 42.4 ± 13.8 at 72 h), and AbLMNVs (9.5 ± 3.9 μg at 24 h, 41.0 ± 2.2 μg at 48 h, and 99.9 ± 10.2 μg at 72 h) with respect to the corresponding plain or functionalized nanovectors incubated without SMF (for LMNVs 2.9 ± 2.2 μg at 24 h; 2.0 ± 0.3 μg at 48 h, $p < 0.05$; and 5.9 ± 0.2 μg at 72 h, $p < 0.05$; for AbLMNVs 0.3 ± 4.1 μg at 24 h, $p < 0.05$; 7.1 ± 0.6 μg at 48 h, $p < 0.05$; and 13.3 ± 1.3 μg at 72 h, $p < 0.05$). It is important to highlight that both the investigated factors (the SMF and the functionalization with the anti-TfR Ab) independently enhanced the BBB crossing, and that the best performances were observed by synergistically exploiting AbLMNVs + SMF for 72 h (99.9 ± 10.2 μg of crossing nanovectors).

The targeting of nanovectors to the GBM spheroids, after the BBB model crossing, was investigated by confocal laser scanning microscopy (CLSM) imaging and flow cytometry at

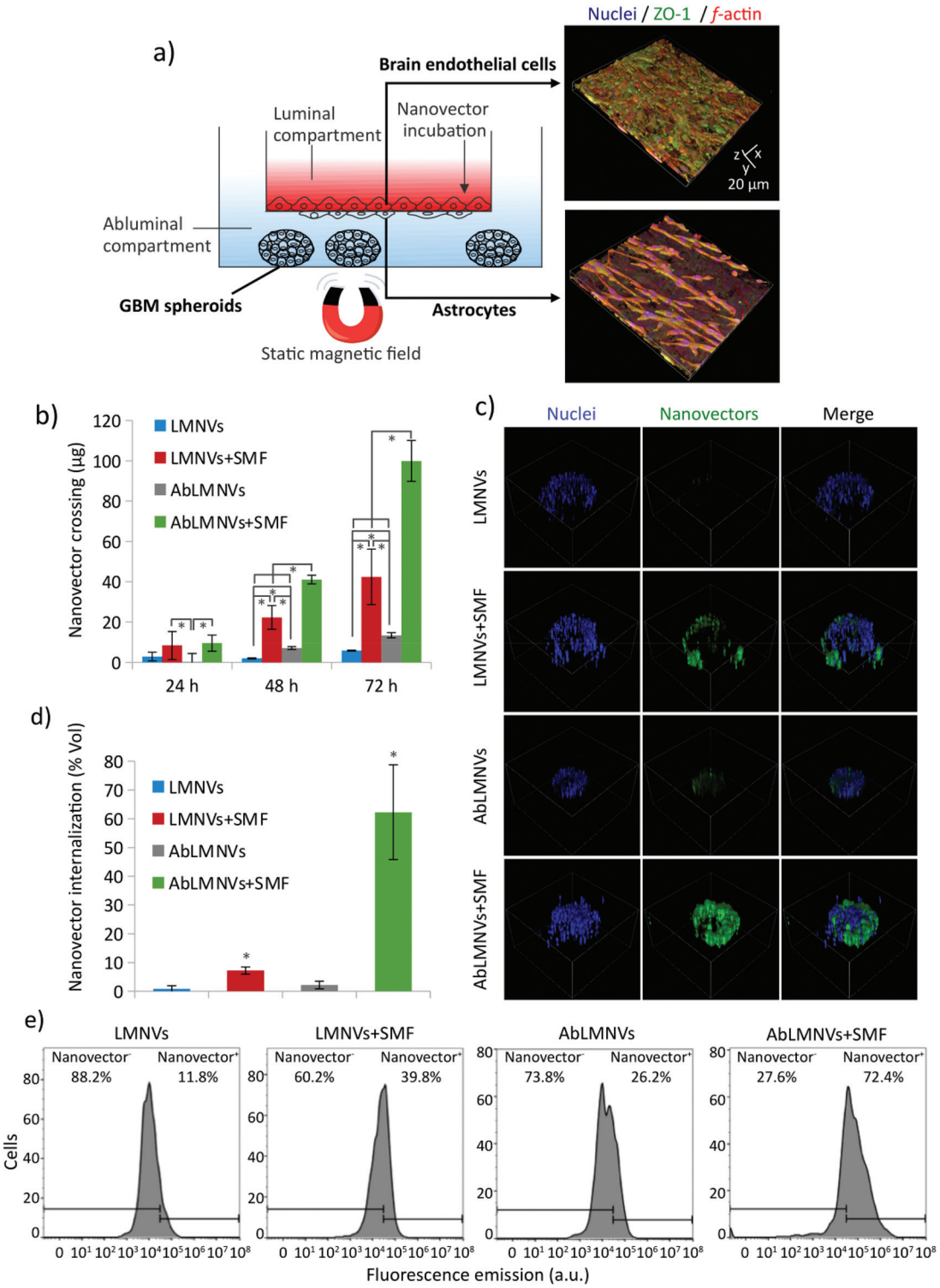

Fig. 2 Blood–brain barrier (BBB) crossing and glioblastoma multiforme (GBM) cell targeting of DiO-stained nanovectors (LMNVs and AbLMNVs) in a multicellular organoid model. (a) Schema of the multicellular model (left) of the BBB (with brain endothelial cells and astrocytes) and of the 3D GBM spheroids; on the right, 3D rendering of fluorescence confocal images of the endothelial monolayer (top) and of astrocytes (bottom; nuclei in blue, ZO-1 in green, and f-actin in red). (b) Nanovector crossing through the BBB in the presence or absence of a static magnetic field (SMF), at different time points (24, 48 and 72 h). The presence of the SMF and the functionalization with anti-TfR Ab are able to independently and synergistically promote the BBB crossing. (c) 3D rendering of fluorescence confocal images of nanovectors targeting the GBM spheroids after BBB crossing (72 h of incubation in the luminal compartment, with or without the SMF); the scan volume is 600 µm (*x* axis) × 600 µm (*y* axis) × 320 µm (*z* axis). (d) Graph showing the percentage of the spheroid volume occupied by nanovectors. (e) Flow cytometry analysis of fluorescence emission of cells dissociated from spheroids, and the corresponding percentage of nanovector-positive (nanovector$^+$) cells.

72 h of treatment. Fig. 2c shows the 3D rendering obtained from CLSM imaging of representative spheroids at 72 h of incubation with LMNVs/AbLMNs in the luminal compartment, in the presence or absence of the SMF. The percentage of the spheroid volume occupied by nanovectors is shown in Fig. 2d; the anti-TfR Ab was able to significantly promote the spheroid targeting in both the presence of SMF (7.2 ± 1.2% for LMNVs + SMF and 62.3 ± 16.5% for AbLMNVs + SMF, $p < 0.05$), and the absence of SMF (0.8 ± 1.1% for LMNVs and 2.2 ± 1.3% for AbLMNV, $p < 0.05$). Similarly to the data collected concerning the BBB crossing, the best results in terms of spheroid targeting were observed by synergistically combining the Ab functionalization with the SMF application ($p < 0.05$). The results obtained with CLSM were then confirmed through flow cytometry by analyzing the fluorescence of the cells dissociated from spheroids (Fig. 2e). A higher percentage of nanovector-positive (nanovector$^+$) cells was observed in AbLMNVs + SMF (72.4%), followed by LMNVs + SMF (39.8%), AbLMNVs (26.2%), and LMNVs (11.8%).

In this experimental configuration, the GBM spheroid targeting efficiency of the nanovectors might be affected by the different levels of their BBB crossing. For this reason, subsequent tests were performed by directly incubating the spheroids with nanovectors at those concentrations that have been found in the abluminal compartment upon BBB crossing. Under these conditions, analysis of nanovector targeting/penetration in GBM spheroids was carried out (Fig. 3). At 24 and 48 h of LMNV/AbLMNV incubation (167 μg ml^{-1}, corresponding to the highest concentration found in the abluminal compartment after 72 h of BBB crossing), CLSM imaging was performed (Fig. 3a); the percentage of the spheroid volume occupied by nanovectors is shown in Fig. 3b. Interestingly, the results indicated that AbLMNVs associated with and internalized in spheroids with improved efficiency with respect to plain LMNVs. Specifically, the percentage of the spheroid volume occupied by AbLMNVs (1.5 ± 0.7% at 24 h and 40.5 ± 2.9% at 48 h) was remarkably higher with respect to that observed for LMNVs (0.8 ± 0.7% at 24 h and 8.1 ± 0.5% at 48 h; $p < 0.05$). The preferential targeting of AbLMNVs was then confirmed by focused ion beam (FIB) milling combined with scanning electron microscopy (SEM; Fig. 3c). Owing to this approach, it has been possible to observe an increased amount of highly electron-dense nanoparticles internalized in the cells inside spheroids when incubated with AbLMNVs with respect to LMNVs. Moreover, the different phases of the nanovector internalization were observed: the nanovector–plasma membrane contact, the cell membrane invagination, and the nanovector internalization in intracellular vesicles (Fig. 3d).

Analysis of the nanovector internalization pathway

We hypothesized that the increased BBB crossing of the functionalized nanovectors with respect to the plain ones could be associated with a different internalization pathway; to test this hypothesis, the analysis of the mechanisms involved in the uptake of plain/functionalized nanovectors by the endothelial cells of the BBB was carried out (Fig. 4). Three different markers expressed in caveosomes (caveolin-1), clathrin-coated vesicles (clathrin) and trancytosis vesicles (rab11) were investigated by CLSM in the endothelial cells of the BBB incubated with LMNVs or AbLMNs (Fig. 4a). CLSM imaging revealed higher intracellular levels of AbLMNVs compared to those of the LMNVs; the enhanced uptake of the functionalized particles by the endothelial cells can be associated with the observed increased level of BBB crossing. Moreover, a relatively high co-localization of the AbLMNV signal with clathrin and rab11 markers can be observed. The quantitative analysis of the Pearson's correlation coefficients is reported in Fig. 4b. A limited internalization of both LMNVs and AbLMNVs in caveosomes was also observed (Pearson's correlation coefficients of 0.03 ± 0.03 for LMNVs and 0.03± 0.05 for AbLMNVs). Increased internalization of AbLMNVs in clathrin$^+$ (Pearson's correlation coefficient of 0.32 ± 0.08) and rab11$^+$ (Pearson's correlation coefficient of 0.54 ± 0.19) vesicles was observed with respect to the non-functionalized LMNVs (Pearson's correlation coefficient: 0.12 ± 0.03 for clathrin, $p < 0.05$; and 0.28 ± 0.03 for rab11, $p < 0.05$). These results indicate that the presence of the Ab on the nanovector surface promotes a clathrin-mediated endocytosis and transcytosis through rab11$^+$ vesicles. Fig. 4c shows SEM images after FIB transverse sectioning of endothelial cells during the uptake of LMNVs (top) and AbLMNVs (bottom).

AbLMNV-assisted magnetothermal stimulation affects GBM cell membrane functionality

The ability of AbLMNV-assisted magnetothermal stimulation to affect plasma membrane functionality was firstly investigated on 2D living cultures of GBM cells (Fig. 5). For these experiments, GBM cultures were incubated with 167 μg ml^{-1} of AbLMNVs, which corresponds to the nanovector concentration that was detected in the abluminal compartment after 72 h of BBB crossing. Firstly, the analysis of intracellular temperature during AMF stimulation was performed at different time points by exploiting an ER-thermo yellow temperature sensor (Fig. 5a and b). ER-thermo yellow is a thermosensitive fluorescent dye, whose fluorescence emission proportionally decreases in response to the temperature increment.[19–21] GBM cultures non-incubated with AbLMNVs that were subjected to AMF were considered as negative controls. A significant decrease of the fluorescence intensity in GBM cells incubated with AbLMNVs was observed (Fig. 5a). The fluorescence (F/F_0) and temperature (T) time courses are shown in Fig. 5b (graphs on the left and on the right, respectively). The temperature levels of the samples stimulated with AbLMNVs + AMF rose from 25 °C until ~41 °C, while an increase of just 2.5 °C was detected in non-incubated negative controls (AMF).

AMF-mediated AbLMNV-assisted magnetothermal stimulation was carried out on GBM cells in the presence of propidium iodide (PI) in the extracellular medium, as an indicator of membrane integrity. In Fig. 5c, the fluorescence and trans-

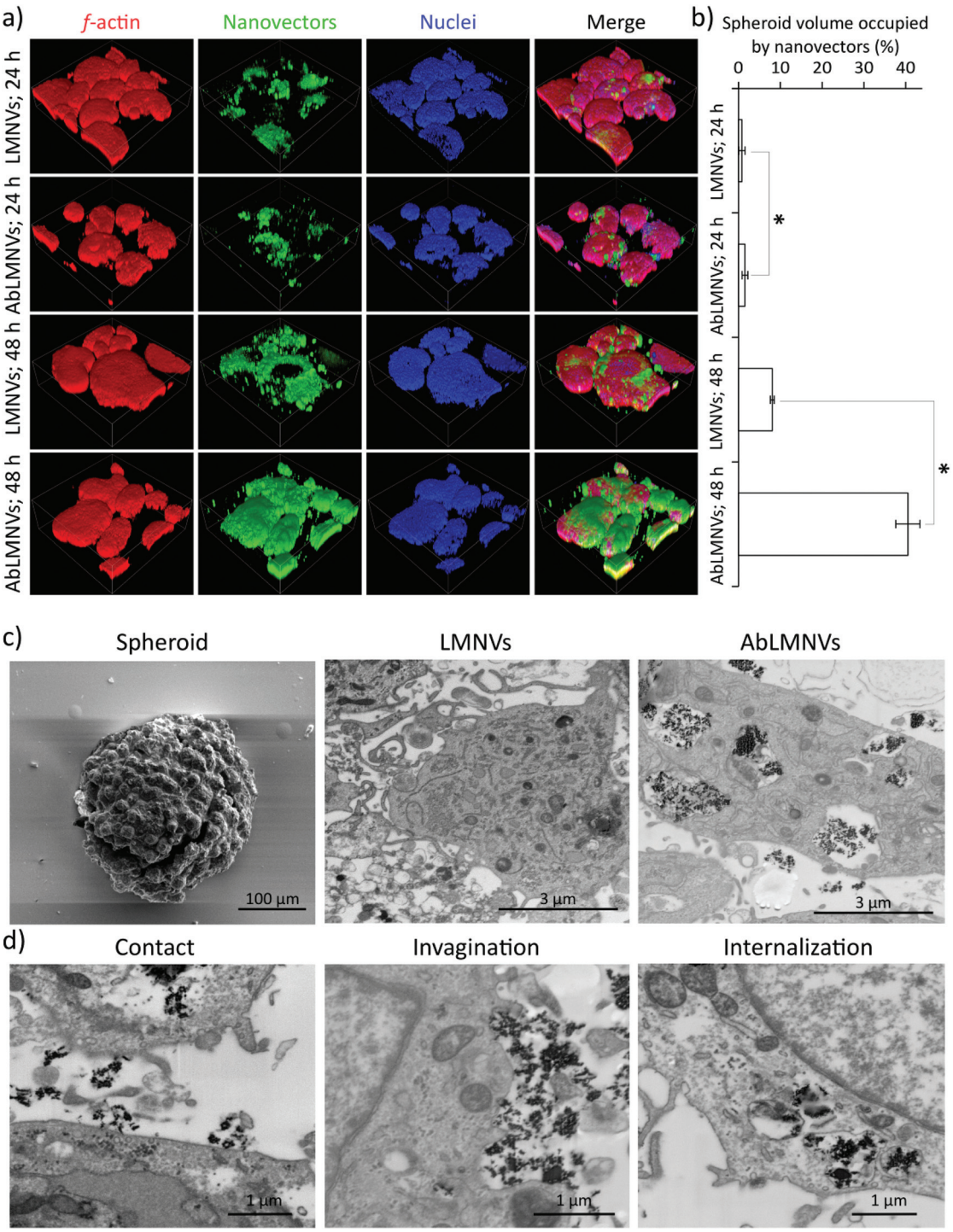

Fig. 3 Nanovector targeting and penetration in spheroids (direct incubation of LMNVs or AbLMNVs in spheroid medium). 3D rendering of fluorescence confocal images of spheroids incubated for 24 and 48 h with DiO-stained LMNVs or AbLMNVs: f-actin in red, nanovectors in green, nuclei in blue; the scan volume is 1270 µm (*x* axis) × 1270 µm (*y* axis) × 185 µm (*z* axis). (b) Graph reporting the percentage of the spheroid volume occupied by the nanovectors. (c) Scanning electron microscopy (SEM) images of a representative spheroid before FIB milling (left); SEM after FIB sectioning of a spheroid incubated for 24 h with LMNVs (middle) or with AbLMNVs (right). (d) FIB-SEM of different phases of the nanovector internalization: the nanovector–plasma membrane contact (left), the cell membrane invagination (middle), and the nanovector internalization in intracellular vesicles (right). * $p < 0.05$.

mitted light images by CLSM are shown for two different time points (t = 0 min and t = 70 min; the AMF stimulus started at t = 12 min). Three different experimental conditions were considered: AbLMNV-incubated cells non-stimulated with AMF (AbLMNVs), cultures non-incubated with AbLMNVs that underwent AMF stimulation (AMF) and cells incubated with AbLMNVs and stimulated with AMF (AbLMNVs + AMF). It is possible to observe cells internalizing the PI during the mag-

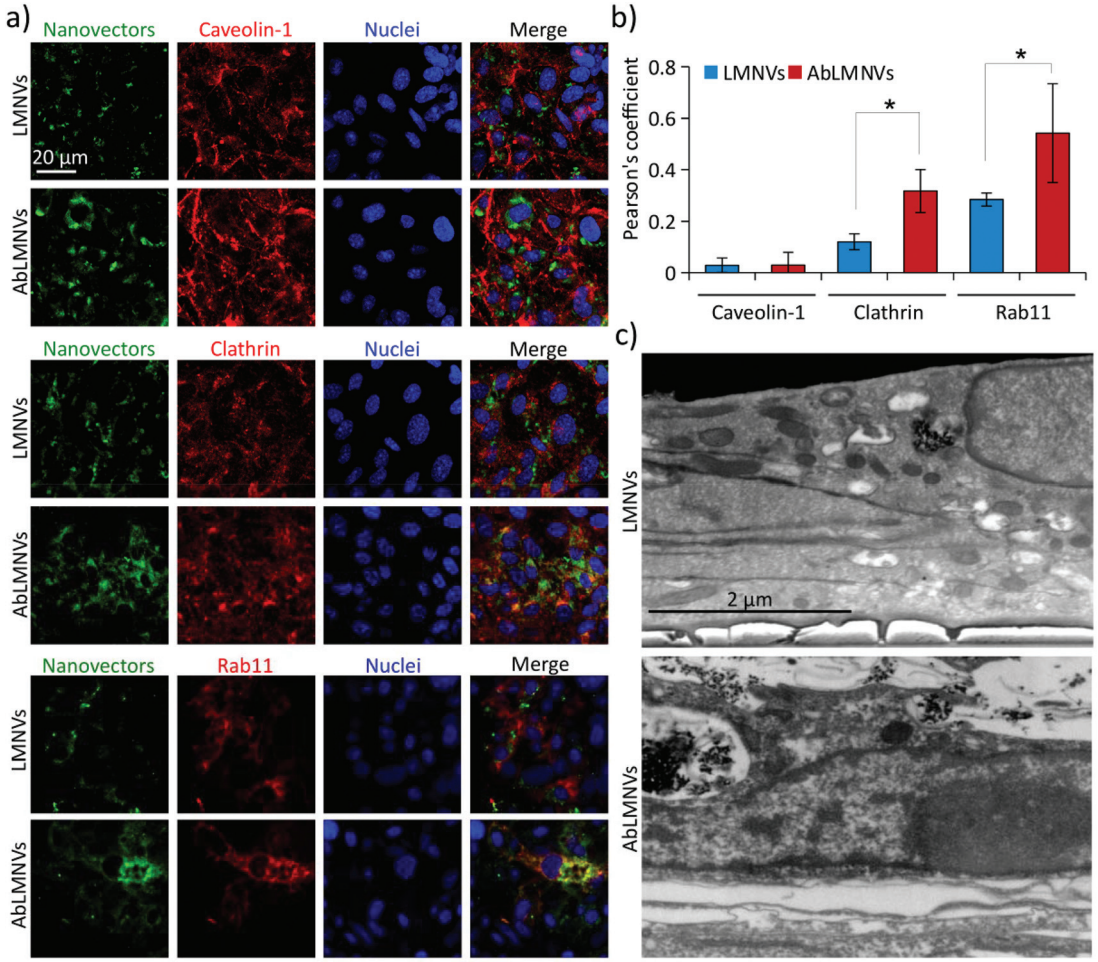

Fig. 4 LMVN functionalization promotes clathrin-dependent endocytosis and transport to transcytosis vesicles. (a) Fluorescence confocal images of caveolin-1, clathrin and rab11 markers (in red) in endothelial cells incubated with nanovectors (DiO-stained LMNVs or AbLMNs, in green); nuclei are shown in blue. (b) Graph reporting the co-localization of the nanovectors with the signals of caveolin-1, clathrin and rab11; * $p < 0.05$. (c) FIB-SEM of endothelial cells during the uptake of LMNVs (top) and AbLMNVs (bottom).

netothermal stimulation generated by the combined AbLMNV + AMF treatment (white arrows); the PI internalization indicates the loss of cell membrane integrity and this is attributable to the temperature increase.[22] Instead, AMF stimulation or AbLMNV incubation did not singularly affect the membrane functionality, highlighting the safeness of this remote stimulation approach. The fluorescence time-lapses of the three experimental conditions are available in the ESI (Videos S1, S2, and S3,† respectively). The fluorescence (F/F_0) time courses relative to PI uptake are reported in Fig. 5d (the black arrow indicates the starting of the AMF stimulus), while the CLSM images of the whole samples at the end of the experiment are shown in Fig. 5e. A remarkable increase of PI^+ cells was observed in response to the magnetothermal AbLMNV + AMF treatment with respect to all the other experimental classes.

Temperature imaging in AbLMNVs in response to AMF

The monitoring of the intraparticle temperature during exposure to AMF was performed by exploiting the temperature-sensitivity of the fluorescence emission spectra of the DiI lipophilic dye (Fig. 6). In Fig. 6a, the emission spectra of DiI in DMSO solution during two temperature cycles are shown (λ_{ex} = 560 nm). The amplitude of the fluorescence emission peak (λ_{em} = 583 nm) linearly decreases in response to the temperature increment; the phenomenon is reversible and the DiI fluorescence emission returns to its original state after subsequent temperature cycles (Fig. 6b). Fluorescence images of the DiI-stained AbLMNVs during heating (ΔT_1 = 0.0 °C; ΔT_2 = 3.5 °C; ΔT_3 = 7.8 °C; ΔT_4 = 10.9 °C; ΔT_5 = 12.3 °C; and ΔT_5 = 14.3 °C) induced by an infrared (IR) laser source are shown in Fig. 6c. The measurement of the temperature increments generated by different laser powers (LP) of the IR source is reported in the ESI (Fig. S3†). The fluorescence intensity (F/F_0) of the DiI-labeled AbLMNVs decreases during heating (Fig. 6d) following a linear relation with the temperature increase ($\Delta F/F_0 = -0.0224 \cdot \Delta T$; R^2 = 0.99; Fig. 6e). In Fig. 6f, the temperature images of the DiI-AbLMNVs internalized into a GBM spheroid before, during, and after the AMF stimulation are shown (the complete time-lapse is available in the ESI, Video S4†). A graph reporting the fluorescence (F/F_0) and the temperature (T) time

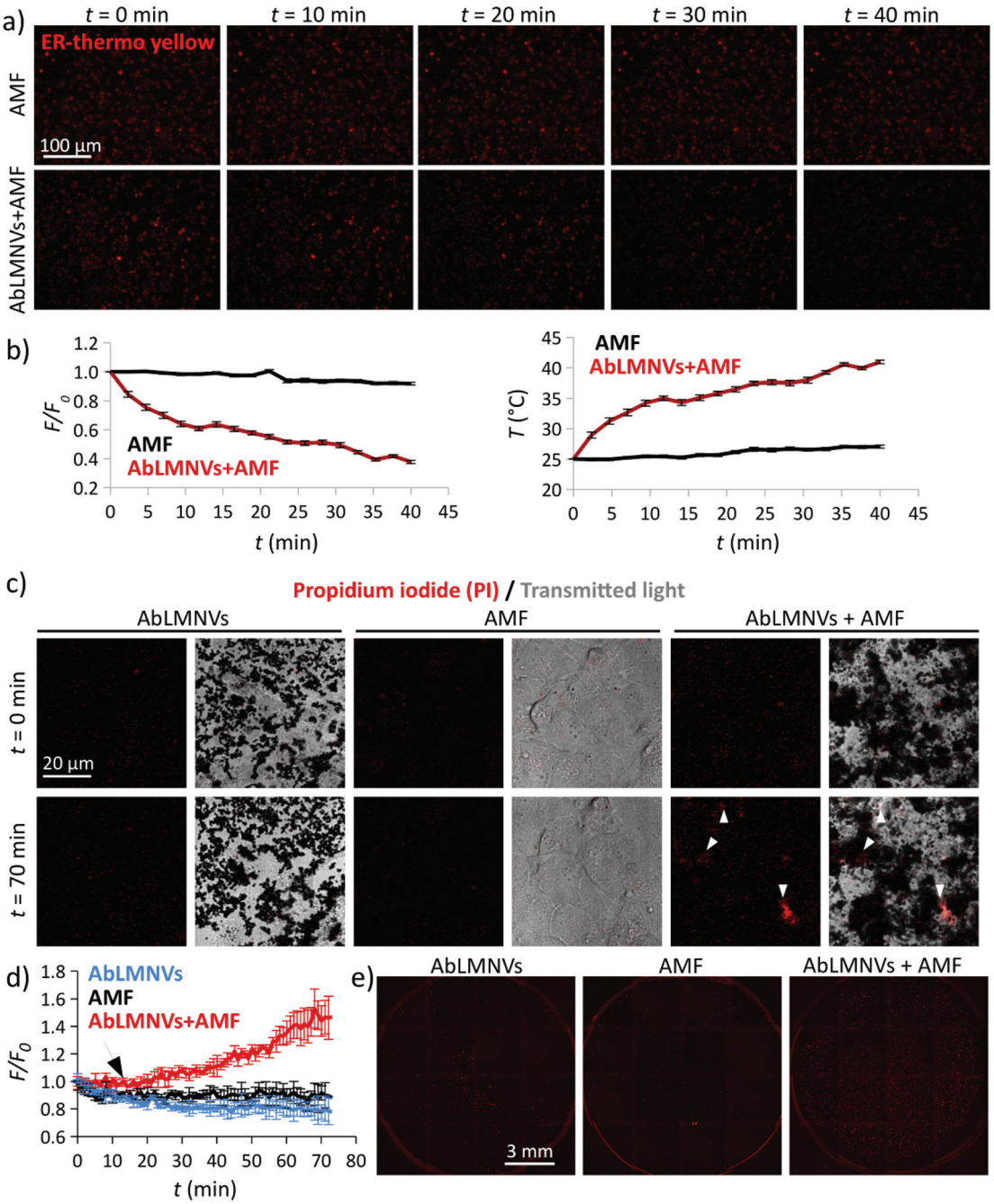

Fig. 5 AbLMNV-assisted magnetothermal stimulation affects plasma membrane integrity in GBM cells. (a) Intracellular temperature imaging during AMF stimulation with the ER-thermo yellow fluorescence thermometer, the fluorescence emission of which proportionally decreases in response to the temperature increment. Representative fluorescence images of GBM cells non-incubated (top) or pre-incubated (bottom) with AbLMNVs that underwent AMF stimulation are reported. (b) The graphs respectively depict the fluorescence (F/F_0; left) and temperature (T; right) time courses for cells non-incubated (black trace) or pre-incubated (red trace) with AbLMNVs, which underwent AMF stimulation. (c) Propidium iodide (PI)/transmitted light imaging before (t = 0 min) and during (t = 70 min) the AMF stimulus (starting at t = 12 min) of AbLMNV-incubated cells non-stimulated with AMF (AbLMNVs), cultures non-incubated with AbLMNVs that underwent AMF stimulation (AMF), and of cultures incubated with AbLMNVs and stimulated with AMF (AbLMNVs + AMF). White arrows indicate the cell internalization of PI due to the loss of cell membrane integrity. (d) PI fluorescence (F/F_0) time courses of the three experimental conditions (the black arrow indicates the starting of the AMF stimulus): AbLMNVs in blue, AMF in black, and AbLMNVs + AMF in red. (e) Fluorescence imaging of the whole samples at the end of the experiment.

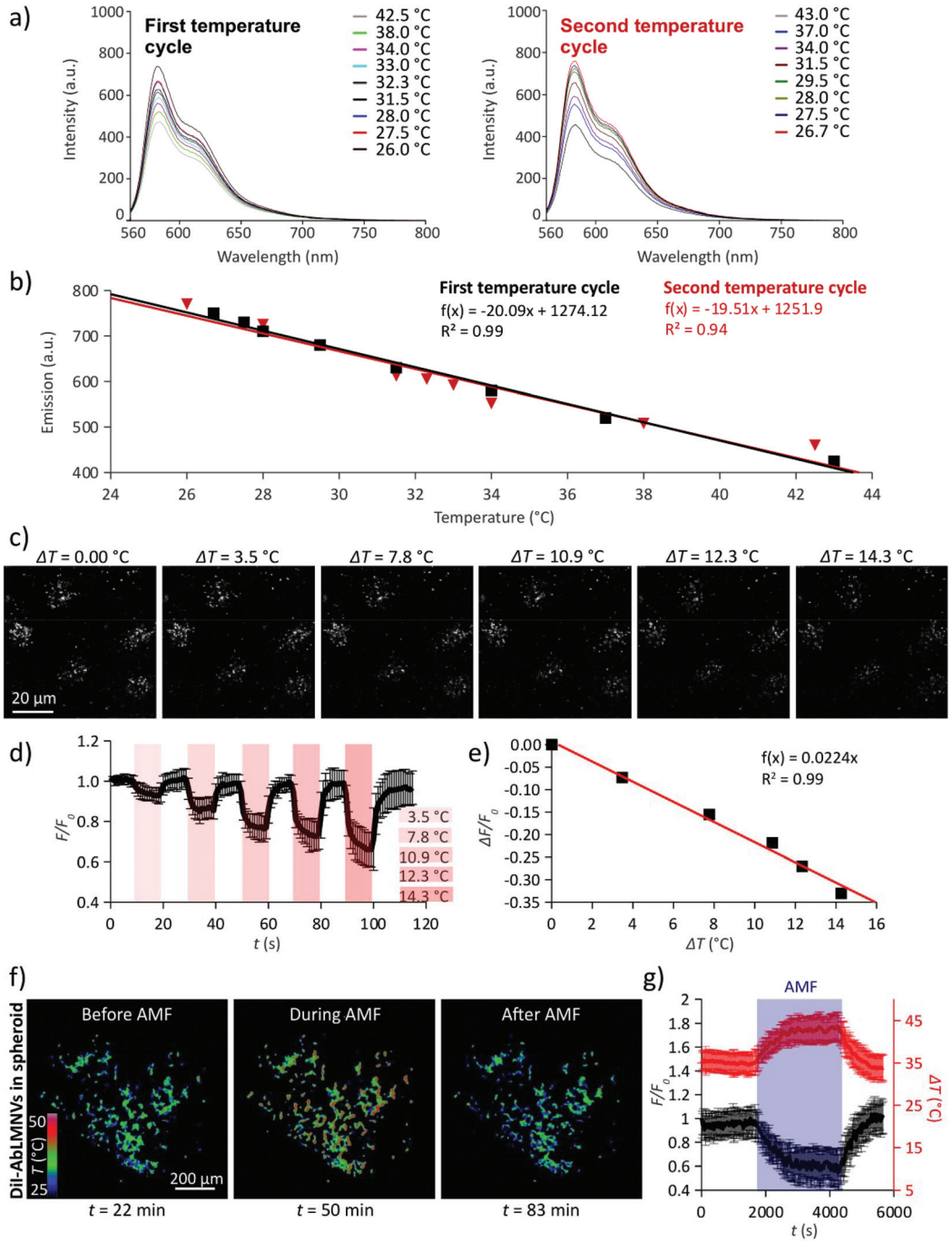

Fig. 6 Intraparticle temperature monitoring during AMF stimulation. (a) Thermosensitivity of fluorescence of the DiI dye in DMSO; fluorescence emission of DiI during two temperature cycles, shown in the left and right graphs, respectively. (b) Linear dependency between the DiI fluorescence emission peak (at λ = 583 nm) and the temperature during the two temperature cycles (shown in black and in red, respectively). (c) Fluorescence imaging of the DiI-labeled AbLMNVs during heating (ΔT_1 = 0.0 °C; ΔT_2 = 3.5 °C; ΔT_3 = 7.8 °C; ΔT_4 = 10.9 °C; ΔT_5 = 12.3 °C; and ΔT_5 = 14.3 °C) induced by an infrared (IR) laser source. (d) Fluorescence intensity (F/F_0) of the DiI-labeled AbLMNVs during heating. (e) Linear relation between $\Delta F/F_0$ and ΔT in DiI-labeled AbLMNVs. (f) Temperature imaging of DiI-labeled AbLMNVs internalized into a GBM spheroid before, during, and after the AMF stimulation. (g) Graph reporting the F/F_0 and the ΔT time course of DiI-AbLMNVs in GBM spheroids during AMF stimulation (the period of AMF exposure is highlighted in blue).

courses of the DiI-labeled AbLMNVs in GBM spheroids during exposure to AMF is shown in Fig. 6g; after 17 min of AMF stimulation, the intraparticle temperature reached and stabilized at ~43.5 °C.

AbLMNV-assisted chronic magnetothermal stimulation induces necrosis, apoptosis and tumor spheroid disintegration

Prior to carrying out chronic magnetothermal treatments, spheroids at day 4 of culture under non-adherent conditions

were imaged by CLSM (images are available in the ESI in Fig. S4†) and their equivalent diameter was 315 ± 91 μm. The anticancer effects of AMF stimulation on GBM spheroids were investigated by pre-incubating spheroids with 167 μg ml^{-1} of AbLMNVs (Fig. 7). The temperature of the medium in the proximity of spheroids, pre-incubated or non-incubated with

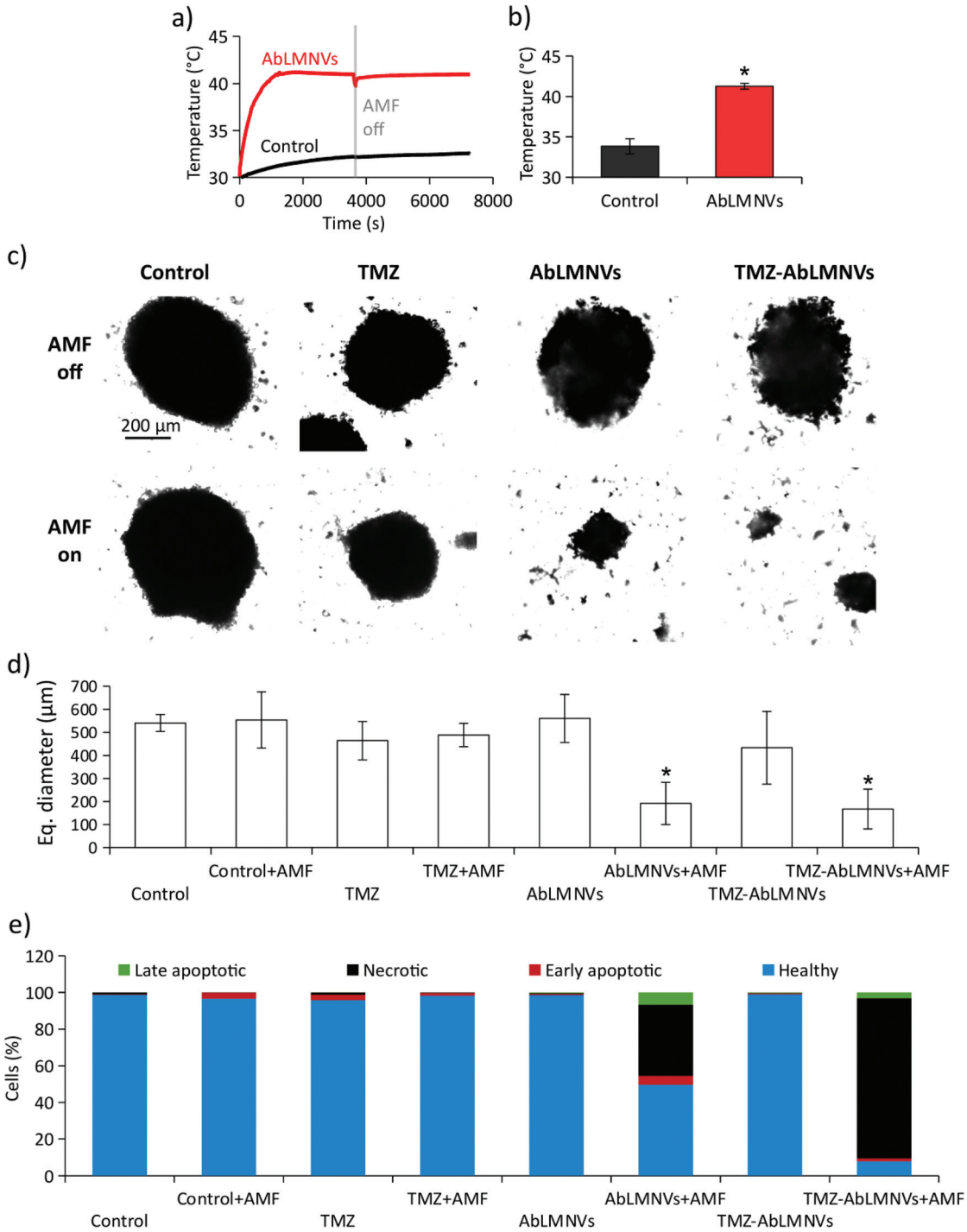

Fig. 7 Disaggregation of GBM spheroids following magnetothermal stimulation and drug treatment. (a) Temperature curves and (b) average temperatures at the equilibrium of the medium in proximity to the spheroids, which were not incubated (control) or pre-incubated (AbLMNVs) with functionalized nanovectors, during AMF stimulation. (c) Transmitted light images and (d) size analysis of non-stimulated (AMF off; top) and stimulated (AMF on; 4 days of chronic treatment, 2 h per day; bottom) spheroids, without pre-incubation with AbLMNVs (control), treated with the drug (TMZ), pre-incubated with AbLMNVs (AbLMNVs), or pre-incubated with TMZ-loaded AbLMNVs (TMZ-AbLMNVs). (e) Plots reporting the percentage of healthy (light blue), early apoptotic (red), late apoptotic (green), and necrotic (black) cells dissociated from the spheroids and analyzed by flow cytometry.

AbLMNVs, was monitored during AMF stimulation by an optical sensor. In Fig. 7a and b, the graphs respectively report representative temperature curves and the average temperatures reached at the equilibrium. The samples treated with AbLMNVs + AMF underwent a significant increase of temperature, which stabilized at 41.3 ± 0.4 °C. A small increase of temperature ($\Delta T \sim 2.5$ °C) was instead recorded for samples stimulated with AMF without pre-incubation with AbLMNVs.

Chronic AMF stimulations (2 h per day for 4 days) were carried out on GBM spheroids non-incubated with AbLMNVs (control + AMF), treated with TMZ (TMZ + AMF), treated with AbLMNVs (AbLMNVs + AMF) or treated with TMZ-loaded AbLMNVs (TMZ-AbLMNVs + AMF). These experimental classes were then compared to the corresponding samples non-exposed to AMF (control, TMZ, AbLMNVs and TMZ-AbLMNVs). Concerning the TMZ and TMZ + AMF experimental classes, the free drug concentration was 6.8 μg ml^{-1}, the amount of TMZ loaded in 167 μg ml^{-1} AbLMNVs (TMZ being 4.1 ± 0.5% w/w).[16] Fig. 7c and d respectively show the imaging and size analysis of spheroids after 4 days of treatment. Spheroids that underwent chronic magnetothermal stimulation (both AbLMNV + AMF and TMZ-AbLMNV + AMF samples) resulted in disaggregation, and only a few small groups of cells could be detected; these samples mostly consisted of necrotic debris. Equivalent diameters of spheroids that did not undergo magnetothermal stimulation (540 ± 37 μm for control, 464 ± 83 μm for TMZ, 560 ± 104 μm for AbLMNVs and 433 ± 157 μm for TMZ-AbLMNVs) were higher with respect to the average size before starting the treatment (315 ± 91 μm), indicating that the non-stimulated GBM spheroids grew during the 4 days of experiment, even when treated with TMZ. No significant differences among the spheroid sizes in these experimental classes (control, TMZ, AbLMNVs, and TMZ-AbLMNVs) were found ($p > 0.05$%). Instead, the equivalent diameter detected after the magnetothermal treatment (192 ± 92 μm for AbLMNVs + AMF and 167 ± 86 μm for TMZ-AbLMNVs + AMF) was significantly smaller not only with respect to the other experimental classes ($p < 0.05$), but even when compared to that one of the samples before treatment ($p < 0.05$). In other words, the magnetothermal therapy induced the disaggregation of the GBM spheroids, and the groups of cells after the treatment became significantly smaller, in terms of their equivalent diameters, with respect to the spheroids at the starting of the experiment.

The viability of the cells in the spheroids after magnetothermal treatment was moreover investigated. Cells dissociated from GBM spheroids were stained with PI/FITC-annexin V and, subsequently, the percentage of healthy, apoptotic, and necrotic cells was analyzed by flow cytometry (Fig. 7e). The plot highlights that the best anticancer results were obtained with the TMZ-AbLMNV + AMF group (7.7% of healthy cells, 87.5% of necrotic cells, 1.6% of early apoptotic cells, and 3.2% of late apoptotic cells), followed by the AbLMNV + AMF group (49.6% of healthy cells, 38.8% of necrotic cells, 4.9% of apoptotic cells, and 6.7% of late apoptotic cells). Concerning the other experimental classes, no remarkable apoptotic/necrotic effects were observed, with a percentage of healthy cells ≥96% in all the experimental groups. Scatter plots of a representative experiment for each experimental class is shown in the ESI (Fig. S5†).

Proteomic analysis of synergic magnetothermal and chemotherapy treatment

Proteomic analysis on the combined effect of magnetothermal and chemotherapy treatment has been performed (number of proteins analyzed = 4208); the results are shown in Fig. 8. In these experiments, non-functionalized LMNVs have been used in order not to affect the proteomic profile in the experimental classes treated with nanovectors, due to the presence of the anti-TfR Ab. In terms of the number of differentially represented proteins (DRPs) among experimental classes, the co-action of AMF, TMZ and LMNVs results in the highest number of DRPs, closely followed by the association of AMF with LMNVs. Almost without exceptions, down-regulated proteins outnumber the up-regulated ones. Concerning the effects generated by the single experimental variable, LMNVs elicit the broadest response when taken as a single experimental variable (it should be noted that TMZ-LMNVs were considered a combination of two factors). In comparison, both AMF and TMZ seem to produce wide effects on the proteome only when combined with other treatments. The results are summarized in Table 1. Four different comparisons can be used to study AMF, TMZ or LMNVs separately; we intersected them to produce four-way Venn diagrams. These highlight a comparatively high number of DRPs shared by at least some comparisons of the LMNV diagram, with 52 proteins found at the intersection of all four parental sets. For AMF, the Venn diagram shows a relatively pronounced impact mainly when LMNVs are provided. TMZ promoted important variations in the member of DRPs only when combined with both AMF and LMNVs. Experimental variables can also be investigated to determine whether they were compound factors: we adopted two-way Venn diagrams to study AMF + TMZ, AMF + LMNVs, or TMZ-LMNVs. Fig. 8a shows Venn diagrams.

Concerning the analysis of coherent proteins and second-order intersections, we defined a DRP as coherent if it is systematically either up- or down-regulated at a given intersection. We observed that most of the DRPs shared between different comparisons are coherent. For selected subsets in our Venn diagrams, we reported the number of coherent proteins (Fig. 8a). With AMF + TMZ-loaded LMNVs and AMF + LMNVs being the most relevant compound variables, we also intersected coherent genes yielded by the AMF + LMNV Venn diagram with comparison 8 *vs.* 1, which studies TMZ-LMNVs + AMF; the results are shown in Fig. 8a.

Concerning the gene ontology terms associated with nanopharmacological treatment, coherent DRPs for our second-order intersection between TMZ-LMNVs + AMF and AMF + LMNVs were used to understand which biological dynamics might have taken place in spheroids following the synergic treatments. To do this, we adopted a gene ontology (GO) strat-

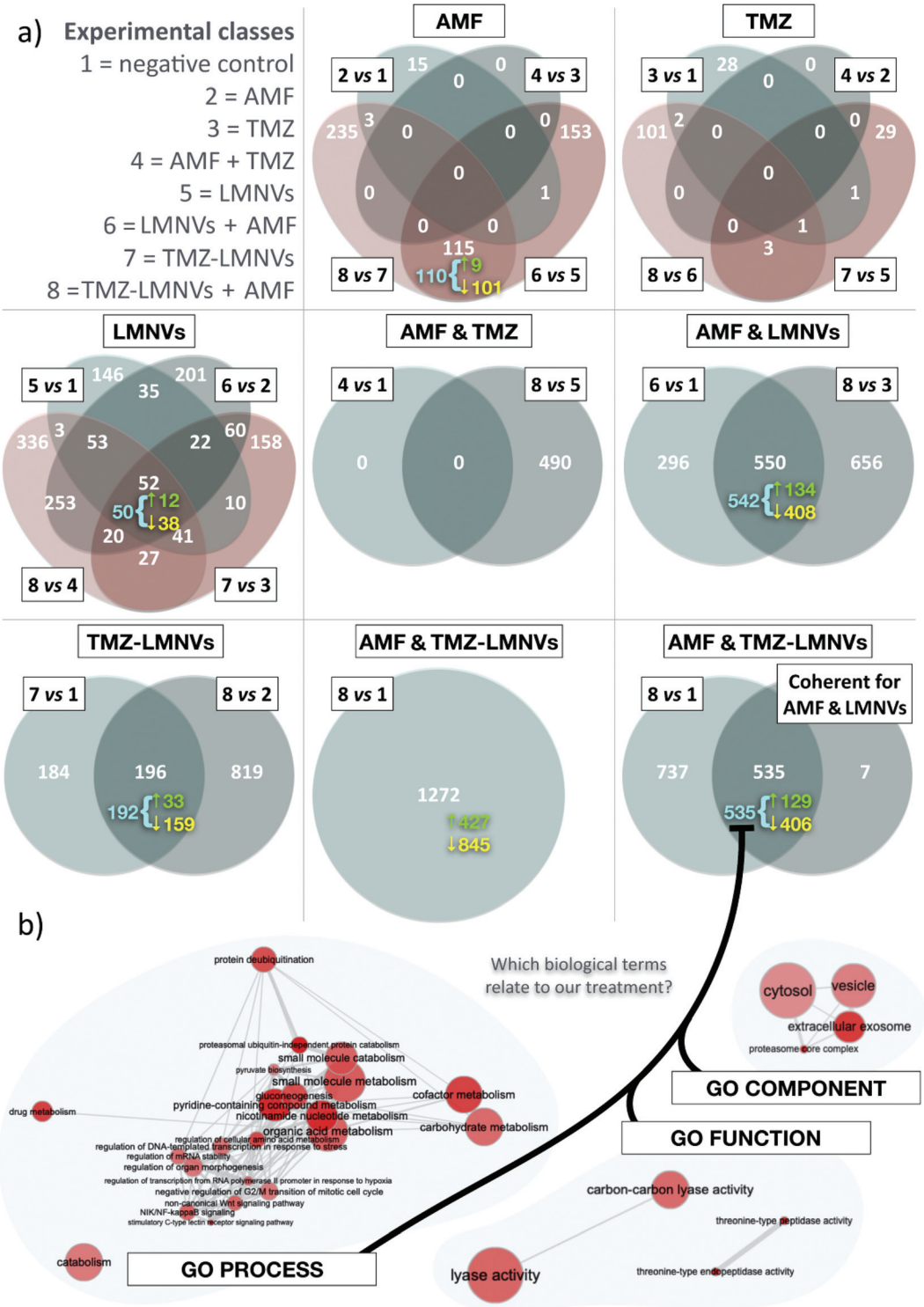

Fig. 8 Apoptotic effects of nanopharmacological treatment are supported by proteomics. (a) Venn diagrams for comparisons among differentially represented proteins (DRPs) for different experimental classes (reported on top, left); AMF = alternate magnetic field; LMNVs = lipid magnetic nanovectors; and TMZ = temozolomide. The number of DRPs in each subset is shown in white; for selected subsets, the amount of coherent DRPs is added below (in cyan). Up- and down-regulated DRPs are also reported for some subsets, respectively in green (preceded by the symbol ↑) or yellow (preceded by the symbol ↓); when coherent DRPs are highlighted, up- and down-regulated proteins refer only to these (as implied by a cyan brace). Experimental variables are evaluated singularly in four-way Venn diagrams (AMF, TMZ or LMNVs); two experimental variables can also be studied as a whole, in two-way Venn diagrams (AMF + TMZ, LMNVs + AMF, or TMZ-LMNVs). The combined effects of TMZ-LMNVs + AMF are shown as a single set; this is also intersected with coherent genes for LMNVs + AMF. (b) REVIGO interactive graphs for gene ontology (GO) term enrichment for biological processes, functions and components, within 535 coherent DRPs found at the intersection between comparison 8 *vs.* 1 and coherent DRPs yielded by the LMNVs + AMF intersection. Single GO terms are represented by red circles, the broadness of which indicates how general a GO term is; color saturation correlates instead with the *p*-value. Gray lines connect similar GO terms, with the line width reflecting the level of similarity. Circle positions also mirror semantic analogies, but these were adjusted as needed for graphical reasons.

Table 1 Differentially represented proteins (DRPs). Number of DRPs for different comparisons (among experimental classes), grouped according to the Venn diagram to which they belong (as depicted in Fig. 8a). DRP compositions in terms of up- and down-regulated factors is also reported

Venn diagram	Comparison	DRPs	Up-regulated	Down-regulated
AMF	2 *vs.* 1	19	2	7
	4 *vs.* 3	0	0	0
	6 *vs.* 5	269	74	195
	8 *vs.* 7	353	90	263
TMZ	3 *vs.* 1	31	19	12
	4 *vs.* 2	0	0	0
	7 *vs.* 5	34	15	19
	8 *vs.* 6	107	52	55
LMNVs	5 *vs.* 1	362	87	275
	6 *vs.* 2	696	186	510
	7 *vs.* 3	390	78	312
	8 *vs.* 4	785	187	598
AMF & TMZ	4 *vs.* 1	0	0	0
	8 *vs.* 5	490	141	349
AMF & LMNVs	6 *vs.* 1	846	250	596
	8 *vs.* 3	1206	382	824
TMZ & LMNVs	7 *vs.* 1	380	76	304
	8 *vs.* 2	1015	282	733
AMF & TMZ & LMNVs	8 *vs.* 1	1272	427	845

egy. GO terms significantly associated with the combined effects of TMZ-LMNVs + AMF were identified for biological processes, functions and components (Fig. 8b). Relevant phenomena are examined in detail in the "Discussion" section.

Magnetothermal stimulation of post-mortem mammalian brain tissue

As a proof of concept, AbLMNVs were injected and exposed to an AMF in a bovine *post-mortem* brain tissue, and temperature was recorded during the experiment (Fig. 9). In detail, 300 μl of a 7 mg ml^{-1} AbLMNV dispersion was injected into the brain tissue (Fig. 9a), transferred into a plastic tube (Fig. 9b), and exposed for 2 h to AMF stimulation. The graph in Fig. 9c shows the temperature levels at the injection site, which reached and stabilized at T = 42.5 °C.

Discussion

In this work, we report for the first time the preparation of lipid magnetic nanovectors functionalized with the anti-TfR Ab (AbLMNVs) for the dual targeting of BBB and GBM cells, and for the combined delivery of magnetothermal stimulation and chemotherapeutic agents (*i.e.*, TMZ). The thermosensitive properties of the DiI lipophilic tracer were investigated and exploited to measure the temperature increase of the lipid matrix of the AbLMNVs in GBM spheroids, which was able to reach 43.5 °C. The disaggregation of TMZ-AbLMNV-targeted GBM spheroids was achieved by chronic exposure to AMF with remarkable anticancer results (92.3% of dead cells, 87.5% of which was necrotic and 4.8% apoptotic).

The enhanced BBB crossing and GBM spheroid targeting achieved with the anti-TfR Ab functionalization of nanovectors were demonstrated through flow cytometry, 3D confocal laser scanning imaging, spectrofluorimetric analysis, and FIB-SEM imaging, by exploiting the high accessibility of the developed multicellular organoid system. The anti-TfR Ab-mediated dual targeting of nanoparticles to endothelial cells of the BBB and to cancer cells has been previously proposed in the literature by independent groups.[23–26] TfR is indeed highly expressed in both endothelial cells of brain vessels and in gliomas;[17,18] TfR is necessary for glioma tumorigenesis, and its expression is indicative of the increased tumorigenicity (2-fold higher TfR expression in grade IV gliomas with respect to lower grade tumors).[18] Both the Tf ligand and anti-TfR Ab have been used to target the TfR; however, considering the quite high concentration of Tf in the blood (1.7–3.7 mg ml^{-1} for humans), the targeting with the anti-TfR Ab is preferable because the Ab does not compete with the endogenous Tf to bind its receptor.[27] Johnsen *et al.* reported that Ab-functionalized gold nanoparticles actively accumulate in brain capillaries and cross the BBB before entering into the brain parenchyma.[27] Furthermore, in another work, Johnsen *et al.* observed that anti-TfR Ab-functionalized immunoliposomes were more efficiently transported to the brain with respect to non-functionalized ones.[28] Here, the brain targeting was successful by using a density of antibodies for a nanoparticle surface of ~8.1

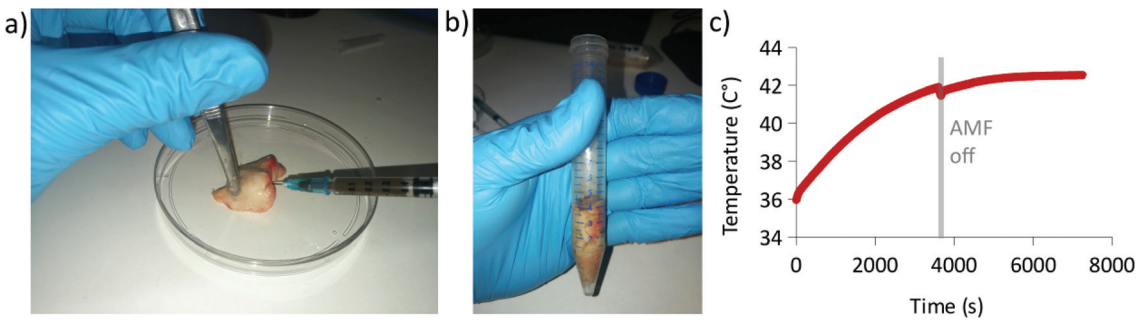

Fig. 9 AbLMNV-assisted AMF-mediated magnetothermal stimulation of a post-mortem animal brain tissue. (a) Injection of 300 μl of a 7 mg ml^{-1} AbLMNV dispersion into the brain tissue. (b) Transfer of the injected tissue in a plastic tube for the AMF stimulation. (c) Graph reporting the temperature levels at the injection site during 2 h of AMF stimulation.

$\times 10^2$ Ab μm^{-2} (considering 50 Ab/immunoliposome and an immunoliposome size of 140 nm), an order of magnitude similar to that of our nanosystem ($\sim 14.8 \times 10^2$ Ab μm^{-2}).

The increased endothelial cell targeting and uptake of the functionalized AbLMNVs were associated with a significantly higher level of endocytosis in clathrin-coated vesicles of these nanovectors with respect to the non-functionalized LMNVs. This result is in line with different pieces of evidence found in the literature, where clathrin-mediated endocytosis resulted in the preeminent internalization pathway for both iron-complexed Tf and TfR-targeting nanoparticles.[29–31] The internalization of both functionalized and non-functionalized nanovectors in caveosomes did not appear significant, probably due to the relatively large size of these nanovectors.[32] Furthermore, a higher amount of AbLMNVs was found in rab11$^+$ vesicles with respect to LMNVs. Rab11 is a small GTPase that prevents the transfer of the cargo to the lysosome compartments, and mediates the transendothelial transport across the BBB.[33,34] Moreover, rab11 regulates the vesicle exocytosis, and the rab11 depletion inhibits tethering and fusion of the TfR$^+$ vesicles to the plasma membrane.[35] Besides TfR targeting, which promotes the increase of nanoparticle crossing through the BBB by a transcellular pathway, other approaches have been proposed to transiently and safely increase the BBB permeability and the consequent paracellular transport of nanoparticles/compounds to the brain. The most relevant examples include the injection of recombinant human vascular endothelial growth factor,[36] the use of focused ultrasound,[37] and the magnetothermal stimulation.[38] In this context, AbLMNV represents a multifunctional nanoplatform which can be locally accumulated with a static magnetic field, is able to promote dual targeting towards both the endothelial cells of the BBB and the GBM cells, and, finally, induces a significant temperature increment when exposed to an AMF; in principle, nanoparticle heating could be exploited, transiently, for promoting the BBB crossing, and, chronically, for GBM treatment.

In this work, we have also reported for the first time the temperature sensitivity of the DiI lipophilic dye. The good thermosensitivity of DiI was then exploited to measure the temperature reached in the lipid matrix of the AbLMNVs in response to an AMF. The temperature inside the particles reached 43.5 °C during the stimulation, slightly higher than that measured in the medium (~41 °C.). Obviously, the equilibrium of the temperature inside the particles and that in solution depends on the average distance of the nanovectors encapsulating the SPIONs and on the localization of the SPIONs inside the nanovectors. A similar finding was also reported by Dong and Zink,[39] who developed mesoporous silica nanoparticles encapsulating SPIONs and $NaYF_4$:Yb^{3+}, Er^{3+} thermosensitive nanocrystals. At the end of the exposure to AMF (frequency of 375 kHz and induction power of 5 kW), the temperature increment of the nanoparticles was two-times higher than that observed in the solution. Beside the reported application of the DiI as an intraparticle thermometer, its good temperature sensitivity and its great affinity with the cell membrane makes this fluorescent probe an interesting tool for monitoring the temperature of the plasma membrane in living cells.

Nanotechnology-based strategies for the temperature-dependent remote control of drug release include the use of near infrared (NIR)-absorbing plasmonic nanomaterials for photothermal conversion and superparamagnetic nanoparticles for a magnetothermal effect, and the ultrasound-induced heating of thermosensitive nanoparticles.[40] Particularly noteworthy in this regard is the recent work of Goodman *et al.*,[41] which demonstrated the NIR-mediated release of a human epidermal growth factor receptor (HER2)-targeted breast cancer drug, lapatinib, from a nanoshell-based human serum albumin protein host complex. Thanks to a femtosecond pulsed laser, the lapatinib was released and induced selective toxicity in HER2$^+$ breast cancer cells without significantly affecting control macrophages. However, the penetration capacity of NIR radiation in biological tissues, although elevated compared to the visible light, is not sufficient to safely treat deep tumors in humans (the incident radiation is reduced to 1/10 at about 2 cm depth and to 1/100 at a 4 cm depth).[42] In contrast, alternating magnetic fields can be efficiently and safely delivered in scarcely accessible deep tissues, such as the human brain.[43] As an example, clinical hyperthermia-based treatments against brain tumors with plain SPIONs have been carried out by the group of Andreas Jordan by exploiting MFH®300F technology (MagForce Nanotechnologies) with a variable field strength of 0–18 kA m^{-1} and a frequency of 100 kHz for the brain delivery of AMF.[44] In our work, the localized heat of nanovectors was exploited for both remotely triggering the TMZ release from nanovectors and for inducing hyperthermia in GMB spheroids. The release profile of TMZ from LMNVs was previously investigated during exposure to AMF;[16] this study was conducted under both lysosome-mimicking conditions (pH 4.5 and 50 μM H_2O_2) and control conditions (pH 7.4 and 0 μM H_2O_2); the results were compared to those of samples non-exposed to AMF. In this previous work we highlighted that, after 3 days of treatment, the lysosome-mimicking conditions slightly affected the TMZ release (4.9 ± 0.1% of cumulative release) with respect to the control (1.0 ± 0.3% of cumulative release), while the chronic AMF stimulation (2 h per day) induced an elevated release of TMZ (65.1 ± 1.9%); the complete release was instead reached after 7 days of chronic magnetothermal stimulation at pH 4.5 with 50 μM H_2O_2. The gradual and remotely controlled drug release from nanovectors can be therefore achieved after repeated applications of AMF.

Concerning the chronic magnetothermal and chemotherapy treatment (TMZ-AbLMNVs + AMF), the biological material resulting after 4 days of stimulation mainly consisted of cell debris, while the small group of cells collected consisted of 92.3% of dead cells (87.5% of necrotic cells and 4.8% of apoptotic cells). The magnetothermal treatment without TMZ (AbLMNVs + AMF) was able to disintegrate the GBM spheroids with a similar efficacy compared to that with TMZ-AbLMNVs + AMF; however, the groups of cells found after the AbLMNV + AMF stimulation were characterized by a higher amount of

healthy cells with respect to those after TMZ-AbLMNV + AMF stimulation. The anticancer effects of TMZ during magnetothermal stimulation (41.9% of increased cell death) were remarkably higher with respect to those induced by TMZ alone. Indeed, treatments of GBM spheroids with free TMZ at the same concentrations loaded in the nanovectors induced low cell death with respect to the controls (+2.8%), while no significant effects on the GBM spheroid size were observed with respect to non-treated controls.

Concerning proteomic analysis, AMF alone seem to have little effect on proteins and to be well tolerated by spheroids (only 19 DRPs of 4208 total proteins were found in AMF *vs.* negative controls). Under our experimental conditions, TMZ also displayed scarce effects in the proteome (only 32 DRPs in TMZ *vs.* negative controls). TMZ appears to elicit a significant response, within our experimental framework, only when delivered *via* LMNVs and just when AMF is also present (1272 DRPs were found in TMZ-LMNVs + AMF *vs.* negative controls). In principle, it is desirable to observe noxious effects from chemotherapeutic agents only in combination with other components of a complex treatment. Hence, we believe that the modest rise in DRPs observed when TMZ is added to LMNVs + AMF is a promising hint of enhanced drug delivery or lethality. A higher number of proteome alterations were instead found in LMNVs with respect to the other single experimental variables (362 DRPs of 4208 total proteins were found in LMNVs *vs.* negative controls). Despite no apoptotic/necrotic and size effects being observed in spheroids treated with plain nanovectors, the higher number of DRPs is compatible with the biological effects of these nanovectors *per se*. However, it should be taken into account that a precise tuning of dosages is beyond the goals of the current study, and remains highly dependent on experimental setups. Similarly, it is worth stressing that our study does not focus on selective toxicity, which continues to be an open question for future investigations. Moreover, synergic effects between AMF and LMNVs, which were compatible with LMNVs heating up upon selective magnetic stimulation, were found (846 DRPs were found in LMNVs + AMF *vs.* negative controls). Sets of DRPs among different experimental classes showed a remarkable degree of coherence. The 535 factors selected through our second-order Venn diagram are all coherent, confirming the general soundness of our approach. When searching for biological phenomena associated with such factors, we enriched in semantic spaces that, overall, are in line with an activation of catabolic pathways preparing spheroids to death. Examples of specific GO terms for biological processes, functions or components are the "stimulatory C-type lectin receptor signaling pathway", "threonine-type peptidase activity", and "proteasome core complex". All these are suggestive of a stress or even apoptotic state.[45,46] The pervasive protein down-regulation observable in our dataset may be a further indication of cell suffering, which could possibly be due to increased transcriptional repression and/or protein catalysis.

Coming back to translational issues, promising clinical outcomes have been achieved by applying the magnetothermal therapy through direct injection of superparamagnetic nanoparticles in GBM tumors. In the context of a first phase I trial, aminosilane-coated SPIONs were stereotaxically injected at a concentration of 112 mg ml^{-1} into the tumors of 14 patients diagnosed with primary or recurrent GBM. The patients underwent 6 sessions of AMF (variable field strength of 2.5–18.0 kA m^{-1} and frequency of 100 kHz), each performed for 60 min, 2 times per week. An average intratumoral temperature of 44.6 °C was observed during AMF applications.[47] In a subsequent phase II clinical trial involving 59 patients with recurrent GBM, a significantly prolonged overall survival (13.4 months) was observed thanks to this treatment.[48] In this context, the magnetothermal stimulation of the *post-mortem* brain tissue directly injected with AbLMNVs was carried out as a proof of concept. Interestingly, mild hyperthermia (42.5 °C) was reached by injecting 0.3 ml of 7 mg ml^{-1} AbLMNVs, a 15-times lower concentration and an 11-times lower volume than the plain SPIONs injected into the GBM patients during the previously mentioned clinical trials. In this regard, it is important to highlight that the lipid matrix where the SPIONs are embedded in AbLMNVs not only has the function of encapsulating the drug for a temperature-dependent controlled release, but also prevents the aggregation/precipitation of SPIONs, therefore guaranteeing the stability of their superparamagnetic behavior and their optimal magnetothermal performances.[49]

Conclusions

The nanoplatform proposed in this work represents an efficient tool for the synergic magnetothermal hyperthermia and chemotherapy treatment of sub-millimetric glioblastoma spheroids: cell populations that, in patients, cannot be surgically resected, resist the current chemotherapy/radiotherapy approaches, and are the main cause of cancer recurrence. The remote activation of lipid magnetic nanovectors by alternating magnetic fields induces the heating of the nanovectors, the chemotherapy drug release, and the hyperthermia-dependent loss of plasma membrane integrity. The single and combined effects of the alternating magnetic fields, lipid superparamagnetic nanovectors, and temozolomide drug on glioblastoma spheroids were deeply investigated. Magnetothermal stimulation without chemotherapy (defined as the combined effect of alternating magnetic fields and lipid superparamagnetic nanovectors) was able to efficiently disintegrate the GBM spheroids; however, only when magnetothermal hyperthermia was combined with the temozolomide treatment (present in the nanovectors at subtoxic doses) the GBM spheroid disintegration was accompanied by significant cell death. When analyzing by proteomics the biological phenomena associated with the combined magnetothermal and chemotherapy treatment, we enriched in semantic spaces that, overall, are in line with the catabolic pathways of cell death (specific gene ontology terms consisting of the stimulatory C-type lectin receptor signaling pathway, threonine-type peptidase activity, and proteasome core complex).

Moreover, the superior abilities of the anti-TfR Ab functionalized nanovectors to overcome the BBB limitation and to target glioblastoma spheroids were preliminarily demonstrated using multi-cellular *in vitro* models. Future investigations will be devoted to test the glioblastoma targeting efficiency and anticancer efficacy of this multifunctional nanosystem on patient-derived orthotopic xenograft models. Concerning the *in vivo* context, although the TfR Ab has been already exploited to efficiently deliver nanoparticles to the brain, TfR is also highly expressed in other organs (especially in the liver), where the nanovectors may accumulate and induce relevant side effects. However, taking advantage of an external static magnetic field, it will be likely to achieve a successful nanovector accumulation in the anatomical region of the brain where the glioblastoma foci are localized. The main scope of our future studies, as previously mentioned, will be focused on the assessment of the effects of the combined magnetothermal and chemotherapy treatment in patient-derived xenograft models characterized by different glioblastoma subtypes, therefore addressing the complex heterogeneity of this type of cancer.

Experimental section

Preparation and functionalization of lipid magnetic nanovectors

Lipid magnetic nanovectors (LMNVs) were fabricated as recently described by our group.[16] Briefly, a mixture of 2.5 mg of oleic acid (Sigma-Aldrich), 25 mg of 1-stearoyl-*rac*-glycerol (Sigma-Aldrich), 2.5 mg of 1,2-dipalmitoyl-*rac*-*glycero*-3-phosphocholine (Sigma-Aldrich), 4 mg of biotin-conjugated PEG-DSPE5k (Sigma-Aldrich), and 84.5 μl of an ethanol solution with superparamagnetic iron oxide nanoparticles (15 wt%; US Research Nanomaterials Inc.) were sonicated at 70 °C until ethanol completely evaporated and lipids melted. After adding 4 ml of a pre-warmed (70 °C) Tween® 80 (Sigma-Aldrich) solution (1.0 wt%) to the mixture, a successive step of ultrasonic homogenization (Fisherbrand™ Q125 Sonicator; amplitude 30%, 120 W, for 20 min) followed by high-pressure homogenization (HPH, EmulsiFlex-B15 from Avestin; 5 repetitions at 100 000 psi) was carried out. After stabilization at 4 °C for 30 min, the nanovectors were purified by centrifugation and washing with ddH_2O (3 times for 30 min at 4 °C). For each preparation, the nanovector concentration was estimated by sacrificing a part of the sample, lyophilizing and weighing it. Temozolomide-loaded nanovectors (TMZ-LMNVs) were obtained with the same procedure described above, by adding 2.5 mg of TMZ to the lipid mixture. Concerning the detailed morphological, physicochemical and magnetic characterization of the LMNVs, it is possible to refer to our previous work, where the TMZ release profiles were also investigated.[16]

The functionalization of nanovectors (both LMNVs and TMZ-LMNVs) with the anti-transferrin receptor antibody (anti-TfR Ab) was achieved by conjugating 30 μl of streptavidin-Ab against TfR (0.5 mg ml^{-1}; Abcore) with 100 μl of a 5 mg ml^{-1} nanovector dispersion containing biotin-PEG-DSPE (with shaking for 1 h at 4 °C), similar to that described for other nanoparticles.[20] The Ab-functionalized nanovectors (respectively named AbLMNVs and TMZ-AbLMNVs) were then purified by dialysis (overnight under stirring with ddH_2O as the eluent; molecular weight cut off: 300 kDa; Spectrum laboratories, Inc.).

For the fluorescence imaging of nanovectors, 100 μl of 5 mg ml^{-1} LMNVs and AbLMNVs were stained with 5 μl of Vybrant DiO (3-octadecyl-2-[3-(3-octadecyl-2(3*H*)-benzoxazolyl-idene)-1-propenyl] perchlorate; ThermoFisher). After 40 min of incubation under shaking, the samples were centrifuged twice (15 000 rpm for 80 min at 4 °C) and the pellet with nanovectors was re-dispersed in ddH_2O. Both the stained and the non-stained nanovectors were centrifuged and dispersed in the complete medium before performing the experiments. The same procedure was carried out for the staining of the AbLMNVs with the lipophilic 1,1′-dioctadecyl-3,3,3′,3′-tetramethylindocarbocyanine perchlorate (DiI; 5 μl of DiI were used for 100 μl of 5 mg ml^{-1} AbLMNVs).

Dynamic light scattering analysis was carried out at 25 °C on a 100 μg ml^{-1} AbLMNV dispersion in water and in complete medium by using a Zeta-sizer NanoZS90 (Malvern Instruments Ltd).

TEM imaging and functionalization analysis

Nanovectors were imaged with a JEOL JEM1011 equipped with a thermionic electron source (tungsten) operating at 100 kV. TEM images were acquired with an 11 Mp Orius 1000 CCD camera (Gatan). To prepare the sample, a 10 μl drop of the solution was drop-cast onto a carbon-coated Cu grid and dried in air. For negative staining, the grid was treated with a 1% uranyl acetate solution for 30 s.

Concerning the analysis of the functionalization efficiency, the samples were diluted with the 4× Laemmli Sample Buffer (Bio-Rad), denatured for 10 min at 95 °C, and then run on a 4–15% Mini-PROTEAN® TGX™ Gel (Bio-Rad) at 100 V for 1 h. The PageRuler™ Plus Prestained Protein Ladder (ThermoFisher Scientific) was run in parallel with the samples. Subsequently, 1 h of staining with Coomassie Brilliant Blue R (Sigma-Aldrich) was carried out. The gel was washed and transferred into MilliQ water for image acquisition. Finally, the band intensities were measured in terms of pixel values by using Fiji software (https://imagej.net/Fiji). The quantity of the Ab in the AbLMNV sample was then calculated using a calibration curve available in the ESI (Fig. S1†).

3D glioblastoma (GBM) spheroids coupled to a multicellular model of the blood–brain barrier

Cancer spheroids were derived from U-87 MG cells (ATCC® HTB-14™) by exploiting the hanging drop approach.[50] The cell medium used consisted of high-glucose Dulbecco's Modified Eagle's Medium (DMEM; Sigma-Aldrich), supplemented with 10% fetal bovine serum (FBS; Gibco), 1% sodium pyruvate, 1% L-glutamine, 1% non-essential amino acids (Gibco), 100 IU

ml^{-1} penicillin (Gibco), and 100 μg ml^{-1} streptomycin (Gibco). 25 μl drops of the cell suspension (1×10^6 cells ml^{-1}) were disposed upside down on lids of 75 mm cell culture dishes to promote cell–cell aggregation (24 h in a humid chamber). Afterwards, the obtained 2D cell aggregates were transferred and cultured for 4 days on 75 mm cell culture dishes precoated with agarose hydrogel (1% in PBS). Spheroids were stained with Hoechst 33342 (1 μg ml^{-1}; Invitrogen), calcein (ThermoFisher) and ethidium homodimer-1 (ethd-1; ThermoFisher), following the standard procedures indicated by the LIVE/DEAD® Viability/Cytotoxicity Kit for mammalian cells (ThermoFisher); 3D imaging of stained spheroids was then performed using confocal laser scanning microscopy (CLSM; C2s system, Nikon) and the equivalent diameter was measured by using the NIS-Elements software (Nikon).

A multicellular *in vitro* model of the blood–brain barrier (BBB) separating a luminal compartment from an abluminal chamber with 3D GBM spheroids was obtained. The BBB model was prepared by firstly seeding C8D1A brain astrocytes (ATCC® CRL-2541™) on the abluminal side of the transwell inserts (3 μm diameter pores; Corning Incorporated) at a density of 2×10^4 cells cm^{-2} and, subsequently, by plating brain-derived endothelioma bEnd.3 cells (ATCC® CRL-2299™) on the luminal side of the inserts at a density of 8×10^4 cells cm^{-2} (the second seeding was carried out ~15 h after the first one). The cells were co-cultured for an additional 4 days by using the same medium composition described for U-87 MG cells. Co-cultures were maintained under a humidified atmosphere, at 37 °C, with 5% CO_2. The barrier functionality was assessed in terms of transendothelial electrical resistance (TEER) with a Millipore Millicell ERS-2 Volt-Ohmmeter, and by analyzing with immunofluorescence the expression of a specific marker of tight junctions, the *zonula occludens-1* (ZO-1); the details of the immunocytochemistry procedures are indicated in the "Immunofluorescence assays" paragraph of the "Experimental section". Finally, for assessing the dual targeting of AbLMNVs, 3D spheroids were transferred to the abluminal compartment of the multicellular BBB model.

Analysis of the blood–brain barrier crossing and of the spheroid targeting

The crossing of DiO-stained nanovectors from the luminal to the abluminal chamber through the multicellular BBB system was investigated in the presence or absence of a static magnetic field (SMF; NdFeB magnet with 10 mm diameter and 8 mm height; 2.9 kg of attraction force; Italfit Magneti S.r.l.); specifically, magnets were fixed under the multicellular system through a custom-made multi-magnet support (Fig. S6†). Subsequently, 160 μg of DiO-stained nanovectors (160 μl of 1 mg ml^{-1} dispersion) were incubated in the luminal compartment of the transwell inserts in the presence or absence of the SMF and the fluorescence of the medium in the abluminal compartment (600 μl) was measured at different time points (24, 48 and 72 h) by using a PerkinElmer Victor X3 multi-plate reader (λ_{ex} = 485 nm, λ_{em} = 535 nm). The fluorescence intensity was then converted to the nanovector concentration thanks to a calibration curve available in the ESI (Fig. S7†). The same experiment was performed with GBM spheroids in the abluminal compartment; after 72 h of nanovector incubation in the luminal compartment, the nanovector fluorescence in the spheroids was assessed by CLSM imaging and flow cytometry. Concerning CLSM, the spheroids were washed twice with PBS, fixed with paraformaldehyde (PFA; 4% in PBS at 4 °C for 25 min) and stained with Hoechst 33342 (1 μg ml^{-1}; Invitrogen); 3D volume analysis of the nanovector signal was performed using NIS-Elements software (Nikon), and the volume occupied by nanovectors was normalized and expressed as % of the spheroid volume. Regarding flow cytometry, the spheroids were washed twice and treated with trypsin for 10 min at 37 °C; subsequently, the spheroids were dissociated to single cells by pipetting, the samples were centrifuged, and finally the cells were resuspended in PBS for flow cytometry analysis of fluorescence emission (Beckman Coulter CytoFLEX; λ_{ex}: 488 nm, λ_{em}: 525 ± 40 nm). The highest value of fluorescence emission in non-treated control spheroids was used for thresholding the population of nanovector-positive cells.

The nanovector targeting to spheroids was moreover investigated by directly incubating spheroids with nanovectors with a concentration of 167 μg ml^{-1} (corresponding to the maximum concentration of nanovectors that was able to cross the BBB). The spheroids were washed twice with PBS, fixed with PFA (4% in PBS at 4 °C for 25 min) and then stained with Hoechst 33342 (1 μg ml^{-1}) and TRITC-phalloidin (100 μM; Millipore). The study of nanoparticle targeting and internalization was then carried out by 3D volume analysis (NIS-Elements software, Nikon), as described above, and by focused ion beam milling combined with scanning electron microscopy (FIB-SEM).

For ultrastructure FIB-SEM imaging, U87-derived spheroids were prepared using the reduced osmium–thiocarbohydrazide–osmium (RO-T-O) ultra-thin plasticization protocol as previously presented.[51,52] Briefly, the samples were fixed in 2.5% glutaraldehyde (Electron Microscopy Sciences, EMS) in 0.1 M sodium cacodylate buffer (EMS) at 4 °C overnight, then washed (3 times for 5 min) in the same buffer and incubated in 20 mM chilled glycine (Sigma-Aldrich) for 20 min. After washing 3 times in chilled buffer, the specimens were post-fixed in a 2% osmium tetroxide (EMS)/1% potassium ferrocyanide (EMS) solution for 1 h on ice (RO step), and then washed 3 times in chilled buffer. During the T step, the samples were incubated with 1% thiocarbohydrazide aqueous solution (EMS) at room temperature for 20 min and washed in distilled water before the incubation with 2% osmium tetroxide aqueous solution (O step) for 1 h at room temperature. To enhance the contrast specimens, the samples were *en bloc* stained overnight at 4 °C in 0.5% uranyl acetate (EMS), washed in chilled deionized water, and incubated in 0.15% tannic acid. After washing 3 times in water at 4 °C, the spheroids were dehydrated by treating at 4 °C with increasing ethanol concentrations (30%, 50%, 75%, 95% and 100%, at 4 °C, 10 min of incubation for each solution). Finally, the samples were infiltrated with increasing concentrations of Spurr's resin (EMS) in

100% ethanol (1 : 3 dilution for 2 h; 1 : 2 for 2 h; 1 : 1 overnight; 2 : 1 for 2 h; and 3 : 1 for 2 h; absolute resin overnight). To remove the excess of resin, each spheroid was mounted in a vertical position for 3 h and washed for a few seconds in absolute ethanol. After the polymerization in an oven at 70 °C, the spheroids were then cut in 4 parts, mounted with colloidal silver paste (RS Company) to a 12 mm pin stub, and sputtered with a 25 nm gold layer. SEM was performed applying a voltage of 3–10 kV and a current of 20–400 pA. A secondary electron (SE) detector was used for the imaging of the whole surface of the spheroids, while backscattered electrons (BSE) were collected for the imaging of the cross sections after FIB milling. A first trench-out was performed by ion milling with the voltage at 30 kV and current at 65 nA. Then, the section was polished by ion beam milling fixing the voltage at 30 kV and the current at 9.3 nA.

Similarly, the brain endothelial bEnd.3 cell line at 24 h of nanovector incubation was fixed with 2.5% of glutaraldehyde (GA; Sigma-Aldrich, 2.5% in ddH_2O for 30 min at 4 °C) and then processed with FIB-SEM as described above for spheroids.

Immunofluorescence assays

The internalization and transcytosis pathway of the nanovectors in the endothelial cells of the multicellular BBB model was investigated by immunostaining of different vesicles involved in the intracellular trafficking. Specifically, the signal co-localization of DiO-stained nanovectors with three markers, caveolin-1, clathrin, and rab11, respectively expressed in caveosomes, clathrin-coated organelles, and transcytosis vesicles, was investigated after 24 h of nanovector incubation. Immunofluorescence staining was carried out as previously described.[53] Briefly, the cells were fixed with PFA (4% in PBS at 4 °C for 25 min), permeabilized with Triton X-100 (Sigma-Aldrich; 0.1% in PBS at room temperature for 25 min) and incubated with blocking solution (10% goat serum in PBS at room temperature for 1 h). For the primary antibody, the samples were treated with primary rabbit anti-clathrin antibody (Abcam; 1 : 200 in 10% goat serum), mouse anti-caveolin-1 antibody (Abcam; 1 : 100 in 10% goat serum), or rabbit anti-rab11 antibody (Abcam; 1 : 100 in 10% goat serum), for 60 min at 37 °C. Afterwards, the cells were washed 5 times with 10% goat serum in PBS and then incubated with a staining solution of 10% goat serum in PBS containing Hoechst 33342 (Invitrogen; 1 : 1000 dilution) and a TRITC-conjugated secondary antibody: a TRITC-conjugated secondary anti-rabbit antibody (1 : 150 dilution; Invitrogen) was used for the staining of clathrin and rab11, while a TRITC-conjugated secondary anti-mouse antibody (1 : 75 dilution; Millipore) was used for staining caveolin-1. Subsequently, CLSM imaging was performed (C2s system, Nikon) and the Pearson's correlation coefficients were calculated with NIS-Elements software (Nikon). The ZO-1 marker expression in the BBB was revealed by immunofluorescence following the same procedures indicated above, with a IgG primary antibody against ZO-1 (1 : 120 dilution; Invitrogen) followed by a staining solution consisting of goat Alexa Fluor 488-IgG anti-rabbit secondary antibody (1 : 200 dilution; Invitrogen), Hoechst 33342 (1 : 1000 dilution; Invitrogen) and TRITC-conjugated phalloidin (100 μM; Millipore).

Cell temperature and propidium iodide time-lapse imaging during acute magnetothermal stimulation

Considering the superior performances of Ab-functionalized nanovectors in BBB crossing and in GBM cell targeting, the following experiments were performed just by using AbLMNVs. The intracellular temperature imaging during stimulation with alternating magnetic fields (AMF) was carried out by using the ER-thermo yellow fluorescence thermometer during fluorescence time-lapse microscopy similar to that described in previous studies.[20,21] Briefly, U-87 MG cells were seeded on WillCo® glass bottom dishes, pre-treated for 24 h with 167 μg ml^{-1} of AbLMNVs, stained with 300 nM ER-yellow, and incubated with phenol red-free HEPES-supplemented complete medium; the samples were positioned on a plastic support of the microscope stage (CLSM C2 system; Nikon), in the center of an electromagnetic coil of a MagneTherm™ equipment (NanoTherics; 16 mT, 753 kHz). CLSM time-lapse imaging was carried out by using a perfect focus system (Nikon) and, in order to prevent objective heating during AMF generation, the microscope revolver was automatically lowered after each acquisition thanks to the escape function (NIS-Elements software); before each acquisition, the revolver was raised up and the perfect focus activated. The same procedures were performed for the control cultures that were not incubated with nanovectors. After fluorescence imaging, the regions of interest (ROI) were thresholded and the fluorescence intensity (F) was measured for each ROI and normalized for the fluorescence intensity at t = 0 min (F_0). The F/F_0 time course was then converted into ΔT (°C) by using a previously reported calibration curve (*i.e.*, an increase of temperature of ΔT = 1 °C corresponds to a fluorescence decrease of $\Delta F = -2.7\%$).[19]

To evaluate the membrane integrity/disruption in response to the AbLMNV-assisted magnetothermal stimulation, three experimental classes were considered: cells pre-incubated with AbLMNVs but not stimulated with AMF, cells non-treated with AbLMNs but stimulated with AMF, and finally cells pre-incubated with AbLMNVs and stimulated with AMF. After 24 h of nanovector treatment, the cells were washed and then incubated with 1.5 μM propidium iodide (PI) in phenol red-free HEPES-supplemented complete medium. The fluorescence time-lapse imaging during AMF exposure was carried out following the same procedures indicated above for the ER-thermo yellow staining. After time-lapse experiments, the acquisition of the whole samples was performed by image stitching through the "Large Image" function (NIS-Elements software, Nikon).

Temperature measurement inside the AbLMNVs in response to AMF

The intraparticle temperature was monitored by using the lipophilic 1,1′-dioctadecyl-3,3,3′,3′-tetramethylindocarbocyanine perchlorate (DiI) fluorescent dye.

Firstly, the temperature sensitivity of the DiI was characterized by measuring the fluorescence emission spectra of the DiI solution in dimethyl sulfoxide (1 : 100 in DMSO) at different temperatures (ranging from 26 to 43 °C) with a spectrofluorimeter (Cary Eclipse fluorescence spectrophotometer, Agilent Technologies). Fluorescence emission spectra were collected during two temperature cycles to evaluate the reversibility of the thermo-sensitive process. Subsequently, U-87 MG cells were stained with ER-thermo yellow or were incubated with 167 μg ml^{-1} of DiI-stained AbLMNVs for 24 h, and then heated with a focused 1475 nm infrared laser. Specifically, the cells were heated to obtain different temperature increments (ΔT_1 = 0.0 °C; ΔT_2 = 3.5 °C; ΔT_3 = 7.8 °C; ΔT_4 = 10.9 °C; ΔT_5 = 12.3 °C; and ΔT_6 = 14.3 °C), induced by increasing IR laser powers (LP; nominal LP were LP_1 = 0 mW; LP_2 = 100 mW; LP_3 = 200 mW; LP_4 = 300 mW; LP_5 = 400 mW; and LP_6 = 500 mW, respectively). During heating, time-lapse fluorescence imaging was performed with a confocal fluorescence microscope (Leica, SP8; HC PL APO CS2 63×/1.40 oil objective lens; 552 nm excitation; 560–647 nm emission) equipped with an IR-LEGO system for heating with a focused IR laser; the fluorescence sensitivity of the DiI-stained particles to the temperature was expressed as a linear function of $\Delta F/F_0$ over ΔT. Finally, the intraparticle temperature measurement was carried out in spheroids pre-incubated for 24 h with 167 μg ml^{-1} DiI-stained AbLMNVs. After incubation, the spheroids were transferred and settled on gelatine-coated WillCo® glass bottom dishes for CLSM imaging during AMF exposure. The values of F/F_0 were finally converted to T depending to the linear temperature sensitivity of the particle fluorescence.

Investigations on apoptosis, necrosis and spheroid size after chronic magnetothermal stimulation

Spheroids were grouped into 8 experimental classes: non-treated controls (w or w/o AMF), and cells treated with AbLMNVs (w or w/o AMF), TMZ-AbLMNVS (w or w/o AMF) or free drug (TMZ, w or w/o AMF). Chronic AMF stimulations were carried out with a MagneTherm™ equipment (NanoTherics; 20 mT, 753 Hz), 2 h per day, for 4 days. During AMF exposure, temperature data were collected by using a fiber optic temperature sensor (Osensa). After 4 days, the spheroids were collected, washed twice in PBS, treated with trypsin (10 min at 37 °C), and dissociated to single cells by pipetting; the samples were centrifuged and cells resuspended in annexin V binding buffer (1×) supplemented with 2.5 μM annexin V-FITC and 1 μg ml^{-1} of propidium iodide (PI). The staining solution was incubated for 15 min at 37 °C protected from light. The fluorescence intensity of the cells stained for annexin V-FITC/PI was evaluated using a Beckman Coulter CytoFLEX (for V-FITC, λ_{ex}: 488 nm and λ_{em}: 525 ± 40 nm were used; for PI, λ_{ex}: 488 nm and λ_{em}: 690 ± 50 nm were used). The percentages of early/late apoptotic, necrotic and healthy cell populations were analyzed using the CytoFLEX software and subsequently reported on column graphs. Moreover, after the chronic treatment, the spheroids were imaged with transmitted light (CLSM; C2 system; Nikon) and their equivalent diameters were plotted on a graph.

Proteomic analysis

Samples were solubilized in 25 μl of 2% sodium deoxycholate (SDC), 40 mM chloroacetamide, 10 mM tris(2-carboxyethyl) phosphine (TCEP) and 100 mM Tris HCl, pH 8, at 100 °C for 10 min and sonicated with a Ultrasonic Processor UP200St (Hielscher), with 3 cycles of 30 s. Lysate samples were digested with 0.7 μg trypsin and 0.3 μg LysC overnight at 37 °C. Then the nanovectors were separated from the samples using a DynaMag-2 magnetic particle concentrator (Invitrogen) and treated with 30 μl of 5% NH_4OH. The supernatant separated from the nanovectors was concentrated and joined with the rest of the sample and processed by the iST protocol.[54]

The samples were analyzed as described in the study by Gaggero *et al.*[55] with few changes. Briefly, the tryptic mixture was loaded from the sample loop directly into a 75 μm ID × 50 cm, 2 μm, 100 Å C18 column maintained at 60 °C and then peptides are separated at a flow rate of 250 nl min^{-1} using a non-linear gradient of 5–45% solution B (75% acetonitrile, 20% H_2O, 5% DMSO and 0.1% formic acid) in 140 min. The eluting peptides were analyzed using an Orbitrap Fusion Tribrid mass spectrometer (ThermoScientific). Orbitrap detection was used for MS1 at a resolving power of 120 K, while Ion Trap detection was used for MS2 measurements with a Rapid Ion Trap Scan Rate. Data dependent MS/MS analysis was performed in top speed mode with a 2 s cycle time, during which precursors detected within the range of m/z 375–1500 were selected for activation in the order of abundance. Quadrupole isolation with a window of 1.8 m/z was used, and dynamic exclusion was enabled for 30 s. Automatic gain control targets were 4×10^5 for MS1 and 1×10^4 for MS2, with 50 and 45 ms maximum injection times, respectively. The signal intensity threshold for MS2 was 1×10^4. HCD was performed using 28% normalized collision energy. One microscan was used for both MS1 and MS2 events. The mass spectrometry proteomics data, containing MaxQuant results, have been deposited at the ProteomeXchange Consortium *via* the PRIDE partner repository with the dataset identifier PXD014652.[56]

MaxQuant software[57] version 1.6.5.0 was used to process the raw data, setting a false discovery rate (FDR) of 0.01 for the identification of proteins, peptides and PSM (peptide-spectrum match); a minimum length of 6 amino acids for peptide identification was required. The Andromeda engine, incorporated into MaxQuant software was used to search MS/MS spectra against the Uniprot human database (release UP000005640_9606 April 2019). In the processing, the variable modifications were Acetylation (Protein N-Term), Oxidation (M), and Deamidation (NQ); in contrast the Carbamidomethylation (C) was selected as a fixed modification. The intensity values were extracted and statistically evaluated using the ProteinGroup Table and Perseus software.[58] The algorithm MaxLFQ was chosen for protein quantification with the activated option "match between runs" to reduce the number of the missing proteins.

Using local scripting, we produced lists of DRPs for each comparison. Three types of lists were generated for every comparison, namely a set of up-regulated proteins, one of down-regulated proteins, and a list containing both types of factors. To study the biological effects of each experimental variable, DRP lists of the latter type were intersected with one another in multiple ways. Experimental classes were named from 1 to 8 (1 = negative control; 2 = AMF; 3 = TMZ; 4 = AMF + TMZ; 5 = LMNVs; 6 = LMNVs + AMF; 7 = TMZ-LMNVs; and 8 = TMZ-LMNVs + AMF). Single variables were AMF, TMZ and LMNVs; each of them was studied by four comparisons, respectively: 2 *vs.* 1, 4 *vs.* 3, 6 *vs.* 5, and 8 *vs.* 7; 3 *vs.* 1; 4 *vs.* 2; 7 *vs.* 5, and 8 *vs.* 6; 5 *vs.* 1, 6 *vs.* 2, 7 *vs.* 3, and 8 *vs.* 4. Each of these sets of four comparisons can be seen as a group of all and only the comparisons that, in different environments, measure the response to a given stimulus. We rendered them as four-way Venn diagrams. Compound variables can be investigated with analogous modalities. These are AMF & TMZ, AMF & LMNVs, and TMZ & LMNVs; they are each represented by two comparisons (4 *vs.* 1 and 8 *vs.* 5, 6 *vs.* 1 and 8 *vs.* 3, and 7 *vs.* 1 and 8 *vs.* 2, respectively), so we illustrated them as two-way Venn diagrams. A further option is provided by the combination of all single variables at once, AMF & TMZ & LMNVs, which was studied by a single comparison (8 *vs.* 1) and is depicted as a simple set.

Concerning the evaluation of coherence and second-order intersections, whenever DRPs were found at any intersection, we evaluated their coherence. Within a given Venn diagram, we defined a protein as coherent only when exclusively up-regulated or exclusively down-regulated in all parent sets generating the subset in which the protein was found. Most relevant proteins were further skimmed by intersecting comparison 8 *vs.* 1 with coherent factors for the other most impactful compound variable. We presented the outcome as a two-way, second-order Venn diagram.

To unveil the GO terms significantly associated with our treatment, we performed GOrilla analyses[59] on all coherent DRPs found at the intersection between comparison 8 *vs.* 1 and the coherent DRPs for a second most relevant compound variable. GOrilla input files were an unranked list of UniProt identifiers for the selected proteins and a background list of all UniProt identifiers within our entire dataset. GOrilla searches were performed for the GO process, GO function and GO component terms. The results were trimmed for significance (on p- and q-values, $\alpha = 0.05$), and sent to REVIGO for final plotting.[60]

Magnetothermal stimulation of post-mortem brain tissue injected with LMNVs

A *post-mortem* brain tissue from cow was purchased from a local butcher and dedicated to an AbLMNV-assisted hyperthermia experiment. 300 μl of a 7 mg ml^{-1} AbLMNV dispersion was injected into a brain tissue of 4.9 g; the sample was then transferred into a 15 ml plastic tube and placed in the center of the electromagnetic coil of the MagneTherm™ equipment (NanoTherics; 20 mT, 753 Hz). The temperature time course was monitored with a fiber optic temperature sensor (Osensa), and the values were reported in a graph.

Statistical analysis

Statistical analyses were performed with *R* software (https://www.r-project.org/). An ANOVA test followed by Tukey's HSD *post-hoc* test was carried out for multiple sample comparisons, while independent *t*-tests were performed in the case of two-sample comparisons. Statistically significant differences among distributions were indicated with * in graphs for $p < 0.05$. Finally, data were plotted in graphs as average ± standard error. Refer to the "*Proteomic analysis*" section for details about the statistical analysis carried out on proteomic data.

Conflicts of interest

There are no conflicts to declare.

Acknowledgements

This work has received funding from the European Research Council (ERC) under the European Union's Horizon 2020 research and innovation program (grant agreement No. 709613, SlaMM; to GC).

Moreover, the Japan Science and Technology Agency (grant number JPMJPR15F5; to MS), the Human Frontier Science Program (grant number RGP0047/2018; to MS), and the JSPS (grant number 15H05931; to YH) are acknowledged.

We finally gratefully thank Professor Young-Tae Chang (Pohang University of Science and Technology, Korea) for kindly providing the fluorescent ER-thermo yellow thermometer.

References

1 A. Tosoni, E. Franceschi, R. Poggi and A. A. Brandes, *Curr. Treat. Options Oncol.*, 2016, **17**, 49.
2 L. P. Ganipineni, F. Danhier and V. Préat, *J. Controlled Release*, 2018, **281**, 42–57.
3 K. Urbańska, J. Sokołowska, M. Szmidt and P. Sysa, *Contemp. Oncol.*, 2014, **18**, 307–312.
4 H. Karabeber, R. Huang, P. Iacono, J. M. Samii, K. Pitter, E. C. Holland and M. F. Kircher, *ACS Nano*, 2014, **8**, 9755–9766.
5 R. Huang, S. Harmsen, J. Samii, H. Karabeber, K. Pitter, E. Holland and M. Kircher, *Theranostics*, 2016, **6**, 1075–1084.
6 C. He, J. Li, P. Cai, T. Ahmed, J. T. Henderson, W. D. Foltz, R. Bendayan, A. M. Rauth and X. Y. Wu, *Adv. Funct. Mater.*, 2018, **28**, 1705668.
7 Z. Chen, F. Liu, Y. Chen, J. Liu, X. Wang, A. T. Chen, G. Deng, H. Zhang, J. Liu and Z. Hong, *Adv. Funct. Mater.*, 2017, **27**, 1703036.
8 E.-K. Lim, T. Kim, S. Paik, S. Haam, Y.-M. Huh and K. Lee, *Chem. Rev.*, 2015, **115**, 327–394.

9 O. L. Gobbo, K. Sjaastad, M. W. Radomski, Y. Volkov and A. Prina-Mello, *Theranostics*, 2015, **5**, 1249–1263.
10 J. Liang, C. Gao, Y. Zhu, C. Ling, Q. Wang, Y. Huang, J. Qin, J. Wang, W. Lu and J. Wang, *ACS Appl. Mater. Interfaces*, 2018, **10**, 30201–30213.
11 D. Ni, J. Zhang, W. Bu, H. Xing, F. Han, Q. Xiao, Z. Yao, F. Chen, Q. He, J. Liu, S. Zhang, W. Fan, L. Zhou, W. Peng and J. Shi, *ACS Nano*, 2014, **8**, 1231–1242.
12 J. Wang, Y. Yang, Y. Zhang, M. Huang, Z. Zhou, W. Luo, J. Tang, J. Wang, Q. Xiao, H. Chen, Y. Cai and X. Sun, *Adv. Funct. Mater.*, 2016, **26**, 7873–7885.
13 S. Laurent, D. Forge, M. Port, A. Roch, C. Robic, E. L. Vander and R. N. Muller, *Chem. Rev.*, 2008, **108**, 2064–2110.
14 D. Bobo, K. J. Robinson, J. Islam, K. J. Thurecht and S. R. Corrie, *Pharm. Res.*, 2016, **33**, 2373–2387.
15 J. Estelrich, M. J. Sánchez-Martín and M. A. Busquets, *Int. J. Nanomed.*, 2015, **10**, 1727–1741.
16 C. Tapeinos, A. Marino, M. Battaglini, S. Migliorin, R. Brescia, A. Scarpellini, C. De Julián Fernández, M. Prato, F. Drago and G. Ciofani, *Nanoscale*, 2018, **11**, 72–88.
17 N. Bien-Ly, Y. J. Yu, D. Bumbaca, J. Elstrott, C. A. Boswell, Y. Zhang, W. Luk, Y. Lu, M. S. Dennis, R. M. Weimer, I. Chung and R. J. Watts, *J. Exp. Med.*, 2014, **211**, 233–244.
18 D. L. Schonberg, T. E. Miller, Q. Wu, W. A. Flavahan, N. K. Das, J. S. Hale, C. G. Hubert, S. C. Mack, A. M. Jarrar, R. T. Karl, A. M. Rosager, A. M. Nixon, P. J. Tesar, P. Hamerlik, B. W. Kristensen, C. Horbinski, J. R. Connor, P. L. Fox, J. D. Lathia and J. N. Rich, *Cancer Cell*, 2015, **28**, 441–455.
19 S. Arai, S.-C. Lee, D. Zhai, M. Suzuki and Y. T. Chang, *Sci. Rep.*, 2014, **4**, 6701.
20 A. Marino, S. Arai, Y. Hou, E. Sinibaldi, M. Pellegrino, Y. T. Chang, B. Mazzolai, V. Mattoli, M. Suzuki and G. Ciofani, *ACS Nano*, 2015, **9**, 7678–7689.
21 A. Marino, S. Arai, Y. Hou, A. Degl'Innocenti, V. Cappello, B. Mazzolai, Y. T. Chang, V. Mattoli, M. Suzuki and C. Ciofani, *ACS Nano*, 2017, **11**, 2494–2505.
22 Y. Yang, Y. Xiang and M. Xu, *Sci. Rep.*, 2015, **5**, 18583.
23 P. Zhao, Y. Wang, X. Kang, A. Wu, W. Yin, Y. Tang, J. Wang, M. Zhang, Y. Duan and Y. Huang, *Chem. Sci.*, 2018, **9**, 2674–2689.
24 D. Raucher, S. Dragojevic and J. Ryu, *Front. Oncol.*, 2018, **8**, 624.
25 T. Kang, M. Jiang, D. Jiang, X. Feng, J. Yao, Q. Song, H. Chen, X. Gao and J. Chen, *Mol. Pharmaceutics*, 2015, **12**, 2947–2961.
26 A. Marino, E. Almici, S. Migliorin, C. Tapeinos, M. Battaglini, V. Cappello, M. Marchetti, G. de Vito, R. Cicchi, F. S. Pavone and G. Ciofani, *J. Colloid Interface Sci.*, 2019, **538**, 449–461.
27 K. B. Johnsen, M. Bak, P. J. Kempen, F. Melander, A. Burkhart, M. S. Thomsen, M. S. Nielsen, T. Moos and T. L. Andresen, *Theranostics*, 2018, **8**, 3416–3436.
28 K. B. Johnsen, A. Burkhart, F. Melander, P. J. Kempen, J. B. Vejlebo, P. Siupka, M. S. Nielsen, T. L. Andresen and T. Moos, *Sci. Rep.*, 2017, **7**, 10396.
29 K. M. Mayle, A. M. Le and D. T. Kamei, *Biochim. Biophys. Acta*, 2012, **1820**, 264–281.
30 S. Xu, B. Z. Olenyuk, C. T. Okamoto and S. F. Hamm-Alvarez, *Adv. Drug Delivery Rev.*, 2013, **65**, 121–138.
31 H. Zhu, B. Zhou, L. Chan, Y. Du and T. Chen, *Int. J. Nanomed.*, 2017, **12**, 5023–5038.
32 P. Foroozandeh and A. A. Aziz, *Nanoscale Res. Lett.*, 2018, **13**, 339.
33 Z. Zhao, A. P. Sagare, Q. Ma, M. R. Halliday, P. Kong, K. Kisler, E. A. Winkler, A. Ramanathan, T. Kanekiyo, G. Bu, N. C. Owens, S. V. Rege, G. Si, A. Ahuja, D. Zhu, C. A. Miller, J. A. Schneider, M. Maeda, T. Maeda, T. Sugawara, J. K. Ichida and B. V. Zlokovic, *Nat. Neurosci.*, 2015, **18**, 978–987.
34 M. De Bock, V. Van Haver, R. E. Vandenbroucke, E. Decrock, N. Wang and L. Leybaert, *Glia*, 2016, **64**, 1097–1123.
35 S. Takahashi, K. Kubo, S. Waguri, A. Yabashi, H. W. Shin, Y. Katoh and K. Nakayama, *J. Cell Sci.*, 2012, **125**, 4049–4057.
36 D. J. Lundy, K. J. Lee, I. C. Peng, C. K. Hsu, J. H. Lin, K. H. Chen, Y. W. Tien and P. C. H. Hsieh, *ACS Nano*, 2019, **13**, 97–113.
37 L. Bai, Y. Liu, K. Guo, K. Zhang, Q. Liu, P. Wang and X. Wang, *ACS Appl. Mater. Interfaces*, 2019, **11**, 14576–14587.
38 M. A. Busquets, A. Espargaró, R. Sabaté and J. Estelrich, *Nanomaterials*, 2015, **5**, 2231–2248.
39 J. Dong and J. I. Zink, *ACS Nano*, 2014, **8**, 5199–5207.
40 Z. Li, E. Ye, David, R. Lakshminarayanan and X. J. Loh, *Small*, 2016, **12**, 4782–4806.
41 A. M. Goodman, O. Neumann, K. Nørregaard, L. Henderson, M. R. Choi, S. E. Clare and N. J. Halas, *Proc. Natl. Acad. Sci. U. S. A.*, 2017, **114**, 12419–12424.
42 G. Ku and L. V. Wang, *Opt. Lett.*, 2005, **30**, 507–509.
43 L. Hwangjae, K. T. Guru, K. Semin and Y. L. Jae, *Nano Res.*, 2018, **11**, 5997–6009.
44 B. Thiesen and A. Jordan, *Int. J. Hyperthermia*, 2008, **24**, 467–474.
45 A. Cambi and C. Figdor, *Curr. Biol.*, 2009, **19**, R375–R378.
46 R. Z. Orlowski, *Cell Death Differ.*, 1999, **6**, 303.
47 K. Maier-Hauff, R. Rothe, R. Scholz, U. Gneveckow, P. Wust, B. Thiesen, A. Feussner, A. von Deimling, N. Waldoefner, R. Felix and A. Jordan, *J. Neurooncol.*, 2007, **81**, 53–60.
48 K. Maier-Hauff, F. Ulrich, D. Nestler, H. Niehoff, P. Wust, B. Thiesen, H. Orawa, V. Budach and A. Jordan, *J. Neurooncol.*, 2011, **103**(2), 317–324.
49 A. K. Gupta and M. Gupta, *Biomaterials*, 2005, **26**, 3995–4021.
50 D. Del Duca, T. Werbowetski and R. F. Del Maestro, *J. Neurooncol.*, 2004, **67**, 295–303.
51 F. Santoro, W. Zhao, L. M. Joubert, L. Duan, J. Schnitker, Y. van de Burgt, H. Lou, Y. Liu, A. Salleo, L. Cui, Y. Cui and B. Cui, *ACS Nano*, 2017, **11**, 8320–8328.
52 X. Li, L. Matino, W. Zhang, L. Klausen, A. F. McGuire, C. Lubrano, W. Zhao, F. Santoro and B. Cui, *Nat. Protoc.*, 2019, **14**, 1772–1802.

53 A. Marino, A. Desii, M. Pellegrino, M. Pellegrini, C. Filippeschi, B. Mazzolai, V. Mattoli and G. Ciofani, *ACS Nano*, 2014, **8**, 11869–11882.
54 N. A. Kulak, G. Pichler, I. Paron, N. Nagaraj and M. Mann, *Nat. Methods*, 2014, **11**, 319–324.
55 S. Gaggero, M. Bruschi, A. Petretto, M. Parodi, G. Del Zotto, C. Lavarello, C. Prato, L. Santucci, A. Barbuto, C. Bottino, G. Candiano, A. Moretta, M. Vitale, L. Moretta and C. Cantoni, *OncoImmunology*, 2018, **7**, e1470730.
56 J. A. Vizcaíno, E. W. Deutsch, R. Wang, A. Csordas, F. Reisinger, D. Ríos, J. A. Dianes, Z. Sun, T. Farrah, N. Bandeira, P. A. Binz, I. Xenarios, M. Eisenacher, G. Mayer, L. Gatto, A. Campos, R. J. Chalkley, H. J. Kraus, J. P. Albar, S. Martinez-Bartolomé, R. Apweiler, G. S. Omenn, L. Martens, A. R. Jones and H. Hermjakob, *Nat. Biotechnol.*, 2014, **32**, 223–226.
57 J. Cox and M. Mann, *Nat. Biotechnol.*, 2008, **26**, 1367–1372.
58 S. Tyanova, T. Temu, P. Sinitcyn, A. Carlson, M. Y. Hein, T. Geiger, M. Mann and J. Cox, *Nat. Methods*, 2016, **13**, 731–740.
59 E. Eden, R. Navon, I. Steinfeld, D. Lipson and Z. Yakhini, *BMC Bioinf.*, 2009, **10**, 48.
60 F. Supek, M. Bošnjak, N. Škunca and T. Šmuc, *PLoS One*, 2011, **6**, e21800.